

## A practical superconducting-microcalorimeter X-ray spectrometer for beamline and laboratory science

W. B. Doriese, P. Abbamonte, B. K. Alpert, D. A. Bennett, E. V. Denison, Y. Fang, D. A. Fischer, C. P. Fitzgerald, J. W. Fowler, J. D. Gard, J. P. Hays-Wehle, G. C. Hilton, C. Jaye, J. L. McChesney, L. Miaja-Avila, K. M. Morgan, Y. I. Joe, G. C. O'Neil, C. D. Reintsema, F. Rodolakis, D. R. Schmidt, H. Tatsuno, J. Uhlig, L. R. Vale, J. N. Ullom, and D. S. Swetz

Citation: [Review of Scientific Instruments](#) **88**, 053108 (2017); doi: 10.1063/1.4983316

View online: <http://dx.doi.org/10.1063/1.4983316>

View Table of Contents: <http://aip.scitation.org/toc/rsi/88/5>

Published by the [American Institute of Physics](#)

---

### Articles you may be interested in

[Laboratory-based high pressure X-ray photoelectron spectroscopy: A novel and flexible reaction cell approach](#)

[Review of Scientific Instruments](#) **88**, 033102033102 (2017); 10.1063/1.4975096

[New density profile reconstruction methods in X-mode reflectometry](#)

[Review of Scientific Instruments](#) **88**, 043503043503 (2017); 10.1063/1.4979513

[Imaging at an x-ray absorption edge using free electron laser pulses for interface dynamics in high energy density systems](#)

[Review of Scientific Instruments](#) **88**, 053501053501 (2017); 10.1063/1.4982166

[Robust regression and its application in absolute gravimeters](#)

[Review of Scientific Instruments](#) **88**, 054501054501 (2017); 10.1063/1.4982953

[High sensitive and high temporal and spatial resolved image of reactive species in atmospheric pressure surface discharge reactor by laser induced fluorescence](#)

[Review of Scientific Instruments](#) **88**, 053107053107 (2017); 10.1063/1.4983060

---



# A practical superconducting-microcalorimeter X-ray spectrometer for beamline and laboratory science

W. B. Doriese,<sup>1,a)</sup> P. Abbamonte,<sup>2</sup> B. K. Alpert,<sup>1</sup> D. A. Bennett,<sup>1</sup> E. V. Denison,<sup>1</sup> Y. Fang,<sup>2</sup> D. A. Fischer,<sup>3</sup> C. P. Fitzgerald,<sup>1</sup> J. W. Fowler,<sup>1</sup> J. D. Gard,<sup>1,4</sup> J. P. Hays-Wehle,<sup>1,5</sup> G. C. Hilton,<sup>1</sup> C. Jaye,<sup>3</sup> J. L. McChesney,<sup>6</sup> L. Miaja-Avila,<sup>1</sup> K. M. Morgan,<sup>1</sup> Y. I. Joe,<sup>1</sup> G. C. O'Neil,<sup>1</sup> C. D. Reintsema,<sup>1</sup> F. Rodolakis,<sup>6</sup> D. R. Schmidt,<sup>1</sup> H. Tatsuno,<sup>7</sup> J. Uhlig,<sup>7</sup> L. R. Vale,<sup>1</sup> J. N. Ullom,<sup>1,4</sup> and D. S. Swetz<sup>1,b)</sup>

<sup>1</sup>National Institute of Standards and Technology, Boulder, Colorado 80305, USA

<sup>2</sup>Department of Physics, University of Illinois, Urbana, Illinois 61801, USA

<sup>3</sup>National Institute of Standards and Technology, Gaithersburg, Maryland 20899, USA

<sup>4</sup>Department of Physics, University of Colorado, Boulder, Colorado 80309, USA

<sup>5</sup>Istituto Nazionale di Fisica Nucleare, Sezione di Milano-Bicocca, Milan, Italy

<sup>6</sup>Argonne National Laboratory, Advanced Photon Source, Argonne, Illinois 60439, USA

<sup>7</sup>Department of Chemical Physics, Lund University, Lund, Sweden

(Received 8 February 2017; accepted 27 April 2017; published online 16 May 2017)

We describe a series of microcalorimeter X-ray spectrometers designed for a broad suite of measurement applications. The chief advantage of this type of spectrometer is that it can be orders of magnitude more efficient at collecting X-rays than more traditional high-resolution spectrometers that rely on wavelength-dispersive techniques. This advantage is most useful in applications that are traditionally photon-starved and/or involve radiation-sensitive samples. Each energy-dispersive spectrometer is built around an array of several hundred transition-edge sensors (TESs). TESs are superconducting thin films that are biased into their superconducting-to-normal-metal transitions. The spectrometers share a common readout architecture and many design elements, such as a compact, 65 mK detector package, 8-column time-division-multiplexed superconducting quantum-interference device readout, and a liquid-cryogen-free cryogenic system that is a two-stage adiabatic-demagnetization refrigerator backed by a pulse-tube cryocooler. We have adapted this flexible architecture to mate to a variety of sample chambers and measurement systems that encompass a range of observing geometries. There are two different types of TES pixels employed. The first, designed for X-ray energies below 10 keV, has a best demonstrated energy resolution of 2.1 eV (full-width-at-half-maximum or FWHM) at 5.9 keV. The second, designed for X-ray energies below 2 keV, has a best demonstrated resolution of 1.0 eV (FWHM) at 500 eV. Our team has now deployed seven of these X-ray spectrometers to a variety of light sources, accelerator facilities, and laboratory-scale experiments; these seven spectrometers have already performed measurements related to their applications. Another five of these spectrometers will come online in the near future. We have applied our TES spectrometers to the following measurement applications: synchrotron-based absorption and emission spectroscopy and energy-resolved scattering; accelerator-based spectroscopy of hadronic atoms and particle-induced-emission spectroscopy; laboratory-based time-resolved absorption and emission spectroscopy with a tabletop, broadband source; and laboratory-based metrology of X-ray-emission lines. Here, we discuss the design, construction, and operation of our TES spectrometers and show first-light measurements from the various systems. Finally, because X-ray-TES technology continues to mature, we discuss improvements to array size, energy resolution, and counting speed that we anticipate in our next generation of TES-X-ray spectrometers and beyond. [<http://dx.doi.org/10.1063/1.4983316>]

## I. INTRODUCTION

A microcalorimeter is a detector that is operated at cryogenic temperatures and measures the energy of an incoming photon or particle via conversion to heat. Microcalorimeters are under development for a variety of spectroscopic applications. They are used over a large range of photon energies from the near-IR<sup>1</sup> (1 eV), to X-rays, to gamma-rays<sup>2,3</sup>

(100s of keV). They are also used to measure the energies of particles (e.g., alpha particles in the 5 MeV range that are emitted in nuclear decays<sup>4</sup>). In addition, microcalorimeters are being developed to perform spectroscopy of the total energy of nuclear decays (so called “*Q* spectroscopy”) in order to measure the neutrino mass.<sup>5–7</sup> In this paper, we focus on the use of microcalorimeters in X-ray spectroscopy in the *soft* (here 250 eV–2 keV) and *hard* (here 2 keV–15 keV) X-ray bands.

X-ray microcalorimeters are relatively small (square detectors with linear sizes of hundreds of  $\mu\text{m}$  are typical) and slow (thermal-decay time constants of hundreds of  $\mu\text{s}$  are

<sup>a)</sup>Electronic mail: doriese@nist.gov

<sup>b)</sup>Electronic mail: swetz@nist.gov

typical) compared to other common, solid-state, X-ray detectors. Thus, in most measurement applications microcalorimeters provide practical collecting area and photon-counting capability only when built into arrays of devices. While many different types of X-ray microcalorimeters, such as magnetic calorimeters<sup>8,9</sup> and silicon thermistors,<sup>10</sup> are presently being pursued, only the transition-edge sensor<sup>11</sup> (TES) has reached the level of maturity in both array fabrication and array readout to allow multi-hundred-pixel arrays of high-resolution, X-ray microcalorimeters to be built and operated routinely.

The best X-ray-TES devices provide eV-scale energy resolution.<sup>12–14</sup> Thus, a multi-hundred-pixel array of X-ray TESs promises to occupy a niche between wavelength-dispersive (WD) and solid-state spectrometers. WD spectrometers (e.g., ruled gratings,<sup>15</sup> Bragg crystals,<sup>16</sup> and various multi-layer structures) can provide exquisite energy resolution but generally have very low collecting efficiency and only narrow-band spectral coverage. Solid-state spectrometers, such as silicon-drift detectors (SDDs) or X-ray charge-coupled-devices<sup>17</sup> (CCDs), on the other hand, provide large collecting areas, can receive high incident X-ray rates, and are inherently broadband, but have relatively poor energy resolution. TES arrays can bridge this gap by providing good energy resolution, large collecting efficiency, broadband spectral coverage, and the ability to receive moderate X-ray fluxes, and thus enable some measurements that cannot presently be performed with other existing spectrometer types. TES spectrometers are especially valuable in observations of dilute and/or radiation-sensitive samples, in time-resolved measurements, and in the “tender” X-ray band of  $\approx 1.5$  keV–3 keV that is difficult to access via WD spectrometers that are based on either gratings or standard (Si, Ge) crystals. In addition, TES spectrometers are becoming commercially available as microanalysis tools on electron microscopes.<sup>18–20</sup> Friedrich<sup>21</sup> compares many types of cryogenic spectrometers to conventional spectrometers for various synchrotron-based spectroscopy measurements, while Uhlig *et al.*<sup>22</sup> compare TESs to WD spectrometers for high-resolution X-ray-emission spectroscopy (XES).

Here, we describe the architecture of a practical X-ray spectrometer, built around an array of TESs, that is intended to be adaptable to a variety of X-ray-science applications. At the time of this submission, our team has deployed seven of these spectrometers to X-ray facilities and laboratory-scale experiments worldwide. Another five are being planned for the near future. These spectrometers share many features, such as the 65 mK detector package, the readout architecture, and a cryogenic system that is designed to be operated by non-experts. In Sec. II, we describe these common elements and the overall design and construction of the spectrometers. Sec. III explains the procedures used to convert the raw data streams (detector current vs. time) from the arrayed sensors to a combined, calibrated, energy spectrum.

The seven deployed and five planned spectrometers are designed for the applications of time-resolved absorption and emission spectroscopy with a tabletop, broadband source,<sup>23–27</sup> synchrotron-based X-ray emission and absorption spectroscopy,<sup>22</sup> synchrotron-based energy-resolved

scattering,<sup>28,29</sup> particle-induced X-ray emission at an accelerator beamline,<sup>30,31</sup> X-ray spectroscopy of hadronic atoms produced by accelerator beamlines,<sup>32,33</sup> metrology of X-ray lines excited by a laboratory tube source,<sup>34</sup> and study of highly ionized atoms and molecules at electron-beam ion traps.<sup>35,36</sup> Sec. IV describes the individual characteristics of each deployed spectrometer, details its intended measurement applications, and summarizes its achieved experimental results. Sec. V describes our next generation of spectrometers that will start making measurements soon.

TES technology is mature enough that we have deployed our first set of spectrometers and they are enabling new measurements now. However, there is still significant, ongoing development and capabilities will continue to expand. Sec. VI discusses anticipated future improvements to the technology and the new measurement capabilities they may allow.

## II. SPECTROMETER DESIGN AND CONSTRUCTION

Here we discuss the design and construction of the spectrometer. Subsections present information about the TES detectors, how arrays of sensors are designed and fabricated, micromachined apertures, time-division-multiplexed readout, the 65 mK detector package, cryogenics, filters and windows, observing geometries, and achieved energy resolution.

### A. TES pixels

An X-ray TES pixel (Fig. 1(a)) consists of a photon absorber and a resistive thermometer (with a combined heat capacity,  $C$ ) that are coupled by a weak thermal link (thermal conductance,  $G$ ) to a cryogenic bath. The absorber converts the energy of an incoming X-ray photon to heat. The thermometer (Fig. 1(b)), a thin film that is voltage-biased into the transition between its superconducting and normal-metal states, transduces this heat into a change in the device resistance and thus the device current. The weak thermal link draws the heat to the bath, thus resetting the device to its quiescent operating state ( $T_{\text{TES}} = T_{\text{op}}$ ,  $R_{\text{TES}} = R_{\text{op}}$ ; see Fig. 1(b)), so it is ready to receive another X-ray photon. The response of the device to an X-ray photon is thus a pulsed decrease in its current that has amplitude of tens of  $\mu\text{A}$  and duration defined by an exponential decay of time constant  $\tau_{\text{TES}} \propto C/G$  that is typically 200  $\mu\text{s}$ –1 ms. Measurement of the amplitude of this current pulse with a SQUID (superconducting quantum-interference device) ammeter in turn allows the measurement of the energy of the X-ray. Known noise sources inherent to the TES are phonon-exchange noise across the weak thermal link and Johnson noise due to the device resistance. In addition, the readout (SQUID and its amplifier chain) can also contribute various types of noise. Many groups around the world make such TES devices and vary the shapes, sizes, materials systems, superconducting critical-temperatures, and absorber geometries based on their own fabrication capabilities and the specific optimizations desired in each device.

The X-ray TES derives its exquisite sensitivity from a low operating temperature ( $T_{\text{op}}$ ), a low heat capacity ( $C \approx 1$  pJ/K,

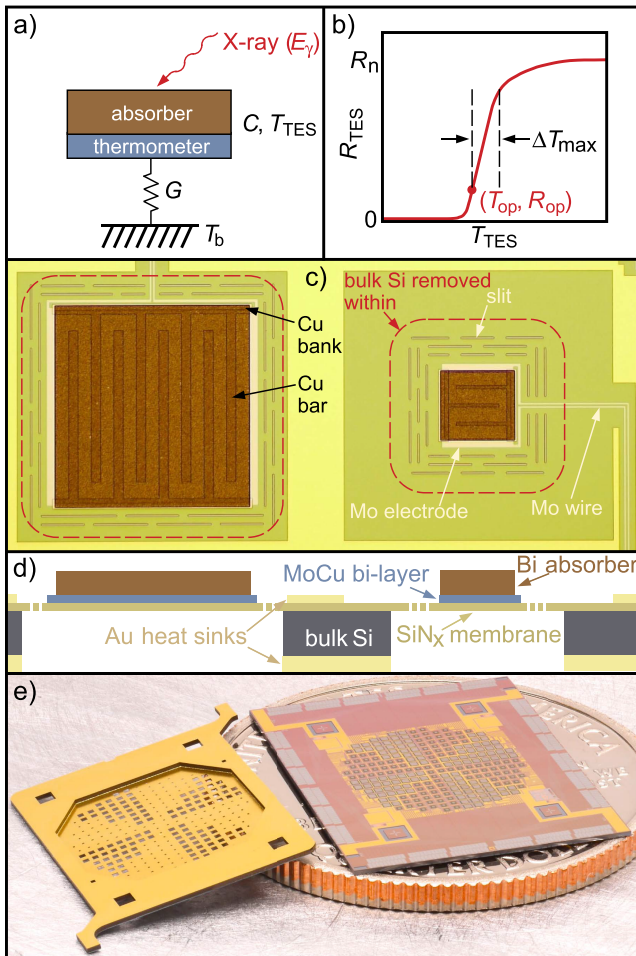


FIG. 1. TES devices. (a) Cartoon schematic of a microcalorimeter, showing the absorber and thermometer (combined heat capacity,  $C$ , operating temperature,  $T_{\text{TES}}$ ), the thermal bath (temperature,  $T_b$ ), and weak link to the bath (thermal conductance,  $G$ ). (b) Cartoon  $R$  vs.  $T$  curve of the TES thermometer. Our devices have normal-state resistance of  $R_n \approx 7 \text{ m}\Omega$ . The superconducting thin film is held in its resistive transition (via voltage bias) at a quiescent operating point of  $R_{\text{TES}} = R_{\text{op}} \approx 0.15R_n \approx 1 \text{ m}\Omega$  and  $T_{\text{TES}} = T_{\text{op}} \approx 107 \text{ mK}$ . The maximum energy the device can sense before saturating is approximately  $E_{\text{max}} \approx C\Delta T_{\text{max}}$ . (c) Annotated micrograph, recorded before the final back-side deep-etch fabrication step, of two TES pixels in a hybrid ar14-type array: a “350  $\mu\text{m}$  device” (left) and a “124  $\mu\text{m}$  device” (right). Devices are named for the linear size of their square TES (MoCu) bilayer. In each pixel, the brown-speckled square is the Bi absorber. Within each dotted-red outline, the bulk Si will be removed from the back via deep etch, leaving each TES suspended on the  $\text{SiN}_x$  membrane to create the weak thermal link. (d) Cross-sectional diagram of the devices pictured in (c); material thicknesses are not to scale. (e) Photograph of a “hybrid” TES array (right) and its micromachined array of apertures (left) with a U.S. quarter-dollar coin for scale. The pictured array contains 240 TES pixels: 120 each of the 350  $\mu\text{m}$  and 124  $\mu\text{m}$  types. During assembly, the aperture chip is aligned to the detector array via micromachined features such that they are separated by about 20  $\mu\text{m}$ .

which is achievable in devices of practical dimensions only at low temperatures), and the sharp change in resistance with temperature in the superconducting transition. The full dependence of the device resistance on its temperature and current is not yet understood, and prediction and control of other device characteristics are areas of active research. TES physics involves both non-equilibrium electrical resistance<sup>37</sup> and the onset of superconductivity at temperatures very near the critical temperature where traditional theories do not hold well.<sup>11,38–40</sup> However, a simple, linear model<sup>41</sup> gives

significant insight into how X-ray TESs are designed for optimal performance. In this model, the TES resistance is expressed as a first-order Taylor expansion in current and temperature about the quiescent operating point,  $(T_{\text{op}}, I_{\text{op}})$ ,

$$R_{\text{TES}}(T_{\text{op}} + \delta T, I_{\text{op}} + \delta I) = R_{\text{op}} + \alpha_I \frac{R_{\text{op}}}{T_{\text{op}}} \delta T + \beta_I \frac{R_{\text{op}}}{I_{\text{op}}} \delta I, \quad (1)$$

where

$$\alpha_I = \left. \frac{\partial \log R}{\partial \log T} \right|_{I_{\text{op}}} = \left. \frac{T_{\text{op}}}{R_{\text{op}}} \frac{\partial R}{\partial T} \right|_{I_{\text{op}}} \quad (2)$$

and

$$\beta_I = \left. \frac{\partial \log R}{\partial \log I} \right|_{T_{\text{op}}} = \left. \frac{I_{\text{op}}}{R_{\text{op}}} \frac{\partial R}{\partial I} \right|_{T_{\text{op}}} \quad (3)$$

are the unitless, partial derivatives with respect to temperature and current that are traditionally used<sup>41</sup> in the TES literature.

In the additional limits of strong electrothermal feedback, low  $T_b$ , and low  $\beta_I$ , the energy resolution is independent of X-ray energy and scales as<sup>41</sup>

$$\Delta E \propto \sqrt{k_B T_{\text{op}}^2 C / \alpha_I}, \quad (4)$$

which suggests that  $T_{\text{op}}$  and  $C$  be made as low and  $\alpha_I$  as high as possible. However, Fig. 1(b) reveals an additional constraint. The linear model is only valid within the superconducting transition in a very limited dynamic range of temperatures,  $T_{\text{op}} \leq T_{\text{TES}} \leq T_{\text{op}} + \Delta T_{\text{max}}$ , where  $\Delta T_{\text{max}}$  is usually on order 1 mK. A TES microcalorimeter is considered to be optimally designed under this modified linear model to achieve the best energy resolution when the linear portion of the transition can just accommodate the highest X-ray energy of interest,  $E_{\text{max}}$ , in a given measurement. This leads to the relation  $E_{\text{max}} = C\Delta T_{\text{max}}$ . Because  $\Delta T_{\text{max}} \propto T_{\text{op}}/\alpha_I$ , in the modified linear model and at a fixed value of  $T_{\text{op}}$ , the ratio  $C/\alpha_I$  is the parameter of primary importance in the design of X-ray TESs.<sup>42</sup> This ratio sets both the energy resolution (as above) and the dynamic range,

$$E_{\text{max}} \propto C T_{\text{op}} / \alpha_I. \quad (5)$$

However, the inclusion of higher-order noise terms related to  $\beta_I$  that are presently understood to arise from the nonlinear and non-equilibrium equivalent to Johnson noise<sup>37</sup> and the experimental observation<sup>43</sup> that devices with higher  $\alpha_I$  also tend to have higher  $\beta_I$  leads to a design space in which lower  $C$  and lower  $\alpha_I$  are chosen for better energy resolution.<sup>42</sup> In these more refined designs,  $\alpha_I$  is usually reduced via normal-metal bars.<sup>12,13,43,44</sup> All devices discussed in this paper use this technique and all have  $\alpha_I < 90$ .

## B. TES arrays

The arrays of X-ray-TES devices described in this paper were fabricated in NIST’s Boulder Microfabrication Facility as follows (see Figs. 1(c)–1(e)). The substrate is a 275  $\mu\text{m}$ -thick, double-side-polished, 3 in. (76.2 mm) Si wafer. First, a 120 nm-thick thermal oxide is grown, followed by 500 nm of silicon nitride ( $\text{SiN}_x$ ) grown via low-pressure chemical-vapor deposition. Layers of Mo (superconductor; 60 nm) and Cu (normal metal; 200 nm) are then deposited via dc-magnetron

sputtering to create a superconducting bi-layer with critical temperature,  $T_c \approx 107$  mK. Variation of the thicknesses of the Cu and Mo layers allows the tuning of  $T_c$  via the proximity effect (see, e.g., Martinis *et al.*<sup>45</sup>). The Cu and then the Mo in this bi-layer are lithographically patterned and then wet etched in separate steps to form Mo wires, electrodes, and wirebond pads connected to square TES-bi-layer pixels of two different linear sizes:  $350 \mu\text{m}$  and  $124 \mu\text{m}$ . An additional  $500$  nm-thick layer of Cu is deposited by electron-beam evaporation and patterned via lift-off lithography to create normal-metal *banks* (used to prevent a superconducting current path along the two non-electrode edges of each sensor) and *bars* (used to control the shape of the superconducting transition as described above); these are pictured in Fig. 1(c). Next, a  $75$  nm layer of Au is electron-beam deposited and then patterned via lift-off lithography to create heat-sinking features at various locations across the array. Then the  $\text{SiN}_x$  is etched to create sets of  $3 \mu\text{m}$ -wide slits to control the thermal conductance ( $G$ ) to the bath. Polycrystalline Bi absorbers of thickness  $2.5 \mu\text{m}$ – $4.1 \mu\text{m}$  are deposited via thermal evaporation and then lift-off lithography. Bi is a semi-metal<sup>46</sup> and so makes almost no contribution to the total  $C$  or the electrical properties of the device. The last front-side step uses the Bosch deep-reactive-ion etch (DRIE) process to create trenches of depth  $20 \mu\text{m}$  that are used to mount the aperture chip. Finally, on the back side of the chip, a thicker ( $1 \mu\text{m}$ ) layer of Au, also to enhance thermalization across the array, is deposited and patterned, and then the DRIE process is used to remove the entire thickness of the Si chip behind each TES.

Table I summarizes the characteristics of the two generations of detector arrays and five unique flavors of pixels used in the spectrometers discussed in this paper. All detector chips are  $15 \times 19 \text{ mm}^2$ . The operating temperature of  $T_{\text{op}} = 107$ – $108$  mK is selected for compatibility with the available cryogenic system (see Sec. II F).

In the first generation of chips, named “ar13,” each chip has 160 detectors. Detector pixels have square TES bilayers of linear size  $350 \mu\text{m}$  and come in three flavors (having 7, 8, and 9 Cu bars). In the ar13 chips, the 160 pixels are on a square grid of pitch  $665 \mu\text{m}$  and are arranged to fit within an overall aperture of diameter  $9.9$  mm (see Fig. 2(a)). All ar13 devices are optimized for the hard X-ray band, with  $E_{\text{max}}$  values near  $10$  keV. We define the *intrinsic* energy resolution of a detector to be the resolution observed at low input X-ray count rates and with non-multiplexed readout so that the readout noise is negligible. The average value of the intrinsic resolution of the ar13 devices is  $\langle \Delta E_{\text{FWHM}} \rangle \approx 2.5$  eV.

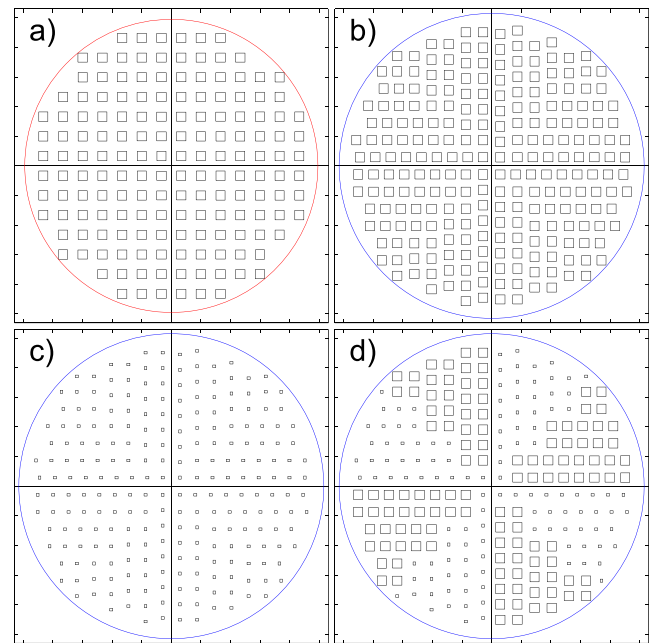


FIG. 2. Detector-plane coverage of the four array types. The smaller rectangles are the  $84 \times 104 \mu\text{m}^2$  apertures for the  $124 \mu\text{m}$  pixels, while the larger rectangles are the  $320 \times 305 \mu\text{m}^2$  apertures for the  $350 \mu\text{m}$  pixels. Small ticks on each axis represent  $1$  mm. (a) ar13-type array with 160 of the  $350 \mu\text{m}$  pixels. The red circle has a diameter of  $9.9$  mm. The apertures fill  $20.3\%$  of the area within this circle. ((b)–(d)) ar14-type arrays with 240 of the  $350 \mu\text{m}$  pixels, 240 of the  $124 \mu\text{m}$  pixels, and 120 of each type. Each blue circle has a diameter of  $10.3$  mm. The apertures of the  $350 \mu\text{m}$  sensors fill  $28.1\%$  and the apertures of the  $124 \mu\text{m}$  sensors fill  $2.5\%$  of the area within this circle.

Detectors with more bars have lower  $\alpha_I$  and thus somewhat higher  $E_{\text{max}}$  and slightly poorer  $\langle \Delta E_{\text{FWHM}} \rangle$ . The ar13 Bi absorbers are of thickness  $2.5 \mu\text{m}$  and provide a quantum efficiency (QE) of  $70\%$  (see the online calculator of Henke *et al.*<sup>47</sup>) at  $6$  keV.

In the second generation of chips, “ar14,” each chip has 240 detectors. There are two flavors of ar14 pixels: (1)  $350 \mu\text{m}$  TESs with 8 Cu bars (optimized for hard X-rays) and (2)  $124 \mu\text{m}$  with 3 bars (optimized for soft X-rays). In the ar14 chips, the 240 pixels are on an irregular grid with an average  $(x, y)$  pitch of  $\approx 520 \mu\text{m}$ . This pattern is intended to maximize the fill factor. The inter-pixel spacing increases farther from the array center, as required to fit the wires that run from each sensor to the chip perimeter. Here, the 240 pixels fit within an aperture of diameter  $10.3$  mm. Due to suspected magnetic impurities introduced at an unknown step during the fabrication process, the heat capacity per unit area of the ar14 devices is almost twice that of the ar13 devices, leading to

TABLE I. Characteristics of the five flavors of TES pixels across two generations of TES arrays. Tabulated values of  $T_{\text{op}}$ ,  $\alpha_I$ , and  $C$  represent averages over measurements of many devices.

Name	Chip gen.	No. of bars	TES lin. size ( $\mu\text{m}$ )	Aperture area ( $\mu\text{m}^2$ )	Thickn. Bi ( $\mu\text{m}$ )	QE( $E$ ) (%)	$T_{\text{op}}$ (mK)	$C$ (pJ/K)	$\alpha_I$	Avg. intrinsic $\Delta E_{\text{FWHM}}$ (eV)	$E_{\text{max}}$ (keV)
ar13-7b	ar13	7	350	$320 \times 305$	2.5	70 (@ 6 keV)	108	0.71	87	2.4 @ 6 keV	9.3
ar13-8b	ar13	8	350	$320 \times 305$	2.5	70 (@ 6 keV)	108	0.72	82	2.5 @ 6 keV	10.0
ar13-9b	ar13	9	350	$320 \times 305$	2.5	70 (@ 6 keV)	108	0.73	77	2.6 @ 6 keV	10.8
ar14-8b	ar14	8	350	$320 \times 305$	4.1	86 (@ 6 keV)	107	1.20	82	3.3 @ 6 keV	16.7
ar14-3b	ar14	3	124	$104 \times 84$	2.8	>99 (<2 keV)	107	0.15	80	1.1 @ 500 eV	2.1

increased dynamic range,  $E_{\max}$ , but at the expense of poorer than intended intrinsic energy resolution of 3.3 eV (average in 8 bars devices at 6 keV) and 1.1 eV (average in 3 bars devices at 500 eV). More recent fabrication tests have indicated a return to the expected values of heat-capacity per unit area (as in the ar13 devices); thus, we expect that future versions of 8 bars devices will return to their excellent performance of 2.5 eV average, intrinsic resolution at 6 keV, and future 3 bars devices will achieve sub-1.0 eV average, intrinsic resolution below 1 keV. The ar14-8b Bi absorbers are of thickness  $4.1 \mu\text{m}$ , which has  $\text{QE} = 86\%$ <sup>47</sup> at 6 keV. The ar14-3b Bi absorbers have a thickness of  $2.8 \mu\text{m}$  and  $\text{QE} > 99\%$  for all  $E < 2 \text{ keV}$ . The ar14 chips have been produced in three types (see Figs. 2(b)–2(d)): (Fig. 2(b)) 240 devices all of size  $350 \mu\text{m}$ , (Fig. 2(c)) 240 devices all of size  $124 \mu\text{m}$ , and (Fig. 2(d)) a “hybrid” array of 120 devices of each of the two sizes. A hybrid array and its aperture chip are pictured separately in Fig. 1(e) and fully assembled in Fig. 3(c).

### C. Aperture arrays

For several reasons, an array of X-ray TESs works best when X-rays strike the chip only on the designated X-ray absorbers. Because the thermal conductance of the bulk Si of the detector chip is not infinite, X-rays absorbed in the Si substrate between sensors are known to create temperature fluctuations seen by nearby sensors and thereby degrade energy resolution. An X-ray absorbed in the  $\text{SiN}_x$  membrane on which each TES is suspended is known to create a different problem: only some of the X-ray energy thermalizes in the detector, while some is shunted directly to the thermal bath (the Si bulk) without first heating the detector, an effect that in turn leads to low-energy tailing in the resultant X-ray spectra. X-rays absorbed in the Mo wiring can drive the wiring from superconducting to normal, thus creating a glitch in the detector data stream that can lead to false triggers. To prevent all of these undesirable effects, we incorporate a micromachined *aperture array* that has, just above each TES, a rectangular opening that is slightly smaller than that of TES’s X-ray absorber.

The aperture arrays are made from a base layer of  $275 \mu\text{m}$ -thick Si. Small epoxy (SU-8) standoffs of height  $40 \mu\text{m}$  are added to the bottom side of the aperture chip. Each detector chip has matching top-side trench features of depth  $20 \mu\text{m}$  (created by the DRIE process) to allow alignment of its aperture chip, creating a net standoff between the aperture and detector chips of  $20 \mu\text{m}$ . The resulting lateral alignment of the aperture chip to the detector chip is  $\pm 5 \mu\text{m}$ . Aperture chips for the 160-pixel ar13 detector chips (see Fig. 2(a)) have no additional metallization, are full-thickness, and are glued to the detector chips with Stycast 2850 epoxy. Aperture arrays for the 240-pixel ar14 detector chips (see Figs. 2(b)–2(d)) come in two different flavors: “wide-angle,” in which all but  $50 \mu\text{m}$  of the bulk Si is removed from the aperture chips’s top side via the DRIE process (see Fig. 1(e)), and full-thickness. In each type of ar14 aperture chip,  $200 \text{ nm}$  of Au is deposited on the top surface to aid in heat sinking. The ar14 aperture chip is not glued to its detector chip, but rather is clipped in place with

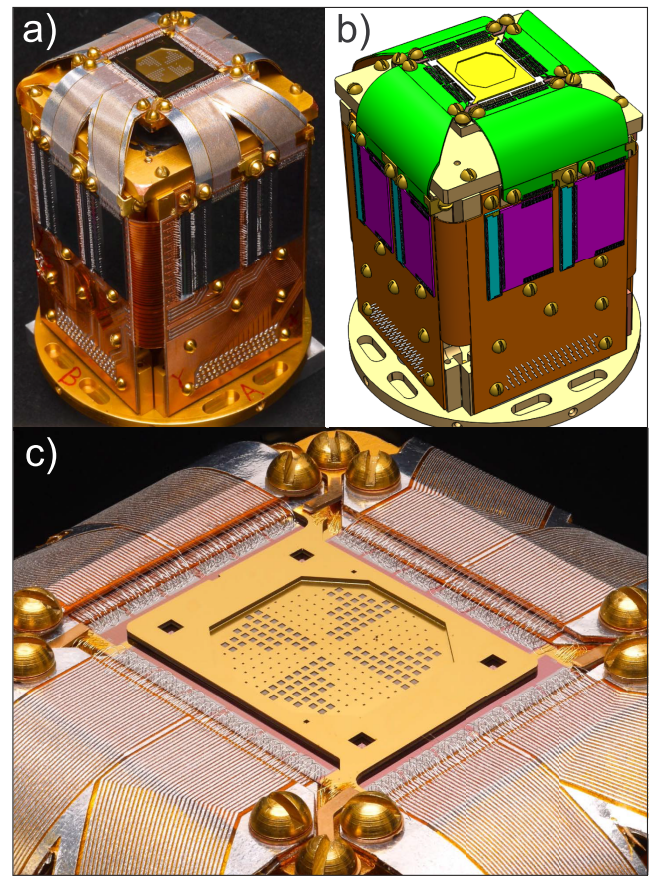


FIG. 3. The 65 mK “snout” package. (a) Photograph of the snout, with hybrid ar14-type array, that was deployed to NSLS. When installed in a spectrometer, the snout is oriented so the detector array (top in this image) faces sideways. The circular pedestal at the bottom of the image has a diameter of  $58.4 \text{ mm}$  and the snout has a length of  $67 \text{ mm}$ . (b) Computer-aided design (CAD) image of the snout, with various parts highlighted in different colors. *Yellow*: The aperture chip sits atop the snout. The interior, octagonal area is thinned to  $50 \mu\text{m}$ . Pixel openings are not shown in this image. The detector array sits just beneath the aperture chip. *Green*: Commercial, flexible circuits with Al wiring. A total of 512 Al traces (256 pairs) run from the detector plane to the four side panels. The Al wires are patterned on a  $200 \mu\text{m}$  pitch from  $25 \mu\text{m}$ -thick foil of Al alloy 5052-O glued to a polyimide substrate, and superconduct below their critical temperature of  $855 \text{ mK}$ . On each of the four sides of the array, two pieces of the flexible circuit are stacked, giving an effective pitch of  $200 \mu\text{m}$  per wiring pair. *Purple*: “Interface chips,” which contain the bias resistors and bandwidth-limiting inductors that make up the detector-bias loops. There are a total of 8 of these chips on the snout, or one for each readout column; each contains biasing circuitry for up to 32 detectors. *Blue*: TDM multiplexer chips. There are eight of these chips total on the snout, or one per readout column. The interface and multiplexer chips are fabricated at NIST. *Brown*: Commercial, rigid-flexible, four-layer Cu printed-circuit board (PCB). This PCB connects to the interface and multiplexer chips via Al wirebonds and carries signals to/from the higher-temperature electronics stages via twisted-pair cables that plug into a trio of 65-lead, “Nano-D” connectors that are on the inside of this PCB. The metallic structure of the snout is machined from oxygen-free-high-conductivity Cu (Cu alloy 101) that has been Au-plated to resist corrosion and aid in thermal conductivity between parts. (c) Higher-resolution photograph of the detector plane of the NSLS snout, showing the aperture chip, detector chip, Al-flexible circuits, and Al and Au wirebonds. For scale, the brass round-head screws are of English size #0-80 (head diameter =  $2.9 \text{ mm}$ ). Reprinted with permission from S. Doyle, “Detectors,” *Synchrotron Radiat. News* **27**, 4 (2014). Copyright 2014 Taylor & Francis LLC (<http://www.tandfonline.com>).<sup>116</sup>

BeCu spring clips and then heat sunk to the thermal bath via Au wirebonds; this scheme is superior in that its heat-sinking path to the thermal bath avoids the detector chip. Thus, high

X-ray fluxes on the aperture chip do not heat the detector chip, which could otherwise cause detector gain to vary undesirably with X-ray flux.

#### D. Time-division-multiplexed readout

In many types of low-temperature detectors, brute-force readout, in which each detector pixel has its own independent amplifier chain and wiring, is only practical in single detectors or in small arrays. Beyond the scale of small arrays, Joule heating from the readout amplifiers and thermal conductance of wires can quickly overwhelm the supporting cryogenic system. Thus, system designers are driven to multiplexed readout, in which signals from multiple detectors are combined into common readout elements. Pursuit of many different types of multiplexed readout schemes<sup>48–51</sup> is an active area of research in the field of low-temperature detectors generally and for X-ray TESs specifically. Multiplexed readout systems for TESs are still generally in the developmental stage, with readout bandwidth and fidelity continuing to increase and readout noise continuing to decrease. These improvements in readout, in turn, allow more and faster sensors, fewer spectral artifacts, and improved energy resolution. Thus, the array sizes and performance specifications detailed in this paper do not represent fundamental limits, but rather will continue to improve as multiplexed-readout techniques evolve.

Here, we use the readout technique of time-division multiplexing<sup>52</sup> (TDM). In TDM, the TESs are dc biased and each TES is coupled to its own first-stage SQUID ammeter. *Rows* of first-stage SQUIDs are turned on sequentially, so that the current signal from one TES at a time per readout column is sampled by the amplifier chain. *Columns* of SQUIDs are read out in parallel. Our present X-ray spectrometers have eight readout columns and either 20 rows (160 TESs in ar13-generation chips) or 30 rows (240 TESs in ar14-generation chips).

The multiplexed readout is controlled by a crate (19-inch-rack, 4u height) of custom-built, high-speed, digital electronics,<sup>53,54</sup> which turns on the first-stage SQUIDs in sequence, controls the operation of the digitally interleaved flux-locked loops<sup>54</sup> that linearize the SQUID responses, and streams data to a computer. All electronics required for a kilopixel-scale (24-column  $\times$  40-row) array can be contained within a single crate. The computer detects X-ray events and stores triggered data to disk. A standard, rack-mounted, dual-quad-core computer is sufficient for all data-acquisition and storage needs. Presently, data analysis<sup>55</sup> (see Sec. III) is performed offline although significant effort is underway to develop real-time processing software.

Each TES's data stream is sampled at a frequency,  $f_{\text{samp}}$ . Higher  $f_{\text{samp}}$  is preferable, as it gives higher-fidelity readout of TESs of a given speed, or allows faster TESs to be read out at a given fidelity level. In the seven presently deployed spectrometer systems (Sec. IV), rows are switched every 320 ns, meaning  $f_{\text{samp}} = 1/(N_{\text{rows}} \cdot 320 \text{ ns})$ . In the 20-row systems,  $f_{\text{samp}} = 156.25 \text{ kHz}$  and in the 30-row systems,  $f_{\text{samp}} = 104.17 \text{ kHz}$ . In the five spectrometers planned for the near future (Sec. V), a newer and more capable generation of the TDM architecture will be used; here the rows are switched every 160 ns (so the

30-row TDM system samples each TES at  $f_{\text{samp}} = 208.33 \text{ kHz}$ ) and the readout noise has also been halved. The SQUID-readout portions of both old and new TDM architectures are described by Doriese *et al.*<sup>56</sup>

#### E. 65 mK detector package

The heart of each spectrometer system is the 65 mK “snout” detector package (pictured and described in Fig. 3). This package contains the TES detector-array chip, aperture chip, biasing circuitry for the TESs and first amplifier stages of the TDM-readout system. The compact size of the 65 mK snout package allows it and its four sets of cylindrical shields (see Sec. II G) to fit through an opening as small as that of a conflat flange of size 6 in. (North American; 6 in. outer diameter of flange) or DN100 (European, Asian; 100 mm bore diameter of flange). The total power load on the 65 mK detector package is summarized in Table II.

#### F. Cryogenics

Our spectrometers employ a common cryogenic architecture. The front end is a two-stage adiabatic-demagnetization refrigerator<sup>57</sup> (ADR), which cools via the magnetocaloric effect<sup>58</sup> as electronic spins in the refrigerant interact with an externally applied magnetic field. The lowest-temperature stage is cooled to the range of  $\approx 65 \text{ mK}$  by an encapsulated “pill” of the refrigerant ferric ammonium alum (FAA), a hydrated paramagnetic salt. The second stage is cooled to the range of  $\approx 650 \text{ mK}$  by a pill of the refrigerant gallium gadolinium garnet (GGG), a paramagnetic-salt crystal. The ADR is backed by a pulse-tube (PT) cryocooler,<sup>59</sup> a closed-cycle mechanical cooler that uses  $^4\text{He}$  as the working fluid and has no moving parts in its cold head. The PT provides two additional thermal stages, of operating temperatures  $\approx 3 \text{ K}$  and  $\approx 50 \text{ K}$ . The combined cryogenic system (described in detail by Bennett *et al.*<sup>2</sup> and now commercially available from multiple vendors) is designed for compactness and ease of operation and produces minimal mechanical vibration and electrical interference. The system requires no liquid cryogenics. Fig. 4 shows a computer-aided design (CAD) rendering of the exterior envelope of the spectrometer (Sec. IV D) installed at beamline U7A of the National Synchrotron Light Source (NSLS-U7A).

The PT cools from room temperature to its base temperature over 16–24 h, and then provides continuous operation

TABLE II. Total power load on the 65 mK detector package. The three power sources are the Joule power of the detector-bias circuitry, the Joule power of the multiplexed-readout circuitry,<sup>56</sup> and thermal conduction through 96 twisted pairs. Each CuNi-clad NbTi signal wire has a free length of 11 cm and a diameter of  $100 \mu\text{m}$ .

Power source	Old TDM architecture power (nW)	New TDM architecture power (nW)
TES bias (8 columns)	5	5
SQUID bias (8 columns)	80	15
96 twisted pairs (total conduction)	10	10
Total	95	30

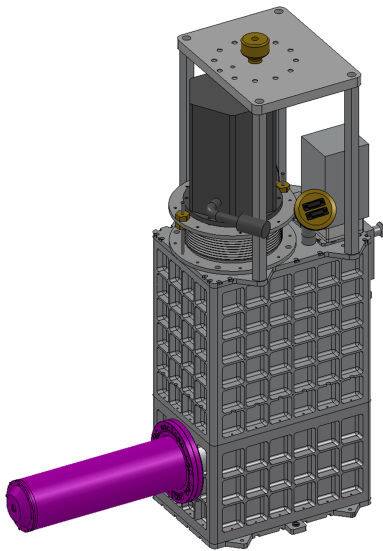


FIG. 4. CAD rendering of the exterior envelope of the NSLS-U7A TES spectrometer. The rectangular body (grey) houses the cryogenic system, and fits in a volume of dimensions 0.91 m tall  $\times$  0.33 m deep  $\times$  0.22 m wide. The detector package is contained within the protruding stainless-steel vacuum shield (purple). Fig. 5 shows the detector protrusion of the NSLS-U7A spectrometer in more detail. Each of the other deployed spectrometers houses its cryogenic system in a similar rectangular body except the NIST-TR spectrometer, which has a cylindrical body of diameter 0.33 m. However, the spectrometers differ widely in the geometry of the protrusion of the detector package, which is customized to mate to its intended measurement apparatus.

at 3 K for a period of months or longer. The ADR provides “single-shot” cooling to 65 mK; the following is a brief description of the cycle. First, a mechanical heat switch connects both ADR stages (FAA and GGG) to the 3 K stage of the PT, and the two refrigerant pills are magnetized isothermally in an applied magnetic field of 4 T. Next, the heat switch is opened and the pills are adiabatically demagnetized and thus cooled from 3 K. The FAA stage reaches a base temperature of about 40 mK. After this, the FAA-stage is servo-ed to a constant temperature of 65 mK ( $\pm 5 \mu\text{K}$  rms) via application of a small control field in the magnet; the field decreases over time to compensate for power dissipated in the FAA stage. When the applied field nears zero, the ADR must be warmed back to 3 K and the cycle is repeated. The re-cycle time (up to 3 K and back down to 65 mK) is typically 2 – 3 h. The FAA-stage servo temperature of 65 mK is chosen based on the desired hold time and the power load (see Table II). Higher ADR-servo temperatures allow longer hold times but result in slightly poorer detector performance. The achieved hold time of 21 h (for a total cycle time synchronized to a 24-h day) at 65 mK is generally convenient for the types of measurements described in Sec. IV.

### G. Shields, windows, and observing geometries

The cryogenics require staged radiation shielding and that the spectrometer be held under vacuum. In addition, the superconducting TES-detector and SQUID-readout elements are magnetically sensitive and so require magnetic shielding. For these reasons, the 65 mK detector package is surrounded by a series of cylindrical shields. From the outside in, these shields are (1) stainless-steel vacuum shield at ambient

temperature, (2) cryogenic mu metal at  $\approx 50$  K to provide magnetic shielding of the detector elements and radiative shielding of the 3 K pulse-tube stage, (3) cryogenic mu metal at  $\approx 3$  K to provide magnetic shielding of the detector elements and radiative shielding of the 65 mK and 650 mK ADR stages, and (4) aluminum (superconducting) at 65 mK to provide magnetic and radiative shielding of the 65 mK detector elements. Each of these shielding stages includes an X-ray transmitting window.

The vacuum window in each system is either a commercial, grid-backed polymer or a thin Be sheet that is designed to support at least 1 atm. Several companies sell such windows. Some of our spectrometers are designed to observe samples in air, while others are inserted into vacuum chambers and observe samples held under vacuum. Even the spectrometers that are designed to operate in vacuum have an atmosphere-supporting vacuum window, in order to protect the spectrometer from a vacuum failure in the beamline and vice versa. The X-ray transmission of the vacuum window is listed at several relevant energies in Table III.

The radiation-blocking windows on the 50 K, 3 K, and 65 mK stages are made of Al and have an open diameter of 17 mm. In the five hard-X-ray spectrometers, each of these three windows is a 5  $\mu\text{m}$ -thick foil. In the two soft-X-ray systems, each of these three is a commercial window that is 100 nm thick, and the outermost of the three has a mesh of fine Ni wires with 95% open area. The combined X-ray transmission through three of each type of Al window is listed in Table III.

Fig. 5 shows a sectioned CAD rendering of the detector protrusion of the NSLS-U7A spectrometer (Sec. IV D). In all spectrometers, the shields are made of the same materials and serve the same purposes; however, they vary among spectrometers in their diameter and length according to the observing geometry required by each experimental apparatus. In our two deployed soft-X-ray synchrotron spectrometers, the detector is entrant through a bellows and gate valve into the

TABLE III. Percent transmission of the vacuum and radiation windows at several X-ray-line energies. Transmission values of the vacuum window given here are the manufacturer’s values for the Luxel LEX-X window; several manufacturers make similar windows with similar transmission values. Each spectrometer also has three cryogenic, Al windows to block infrared radiation. The two spectrometers intended for soft (sub-keV) X-rays are equipped with commercial, 100 nm, Al windows (so, 300 nm of Al total). The outermost of these very thin Al windows, which is held at about 50 K and sees a 300 K blackbody load, has a mesh of fine Ni wires (with 95% open area) to cool the center of the window. The five spectrometers intended for hard X-rays have windows made of 5  $\mu\text{m}$  Al foil; these windows are less expensive and more robust to handling. Transmission calculations of Al are from the online calculator of Henke *et al.*<sup>47</sup> The final column gives the total (percent) transmission through all windows.

Line	Energy (eV)	$T$ (%) vac. win.	$T$ (%) 300 nm Al	$T$ (%) 15 $\mu\text{m}$ Al	$T$ (%) total
C $K\alpha$	275	66	7		5
N $K\alpha$	395	24	34		8
O $K\alpha$	525	44	58		24
Cu $L\alpha$	930	68	89		57
Mn $K\alpha$	5900	82		63	51

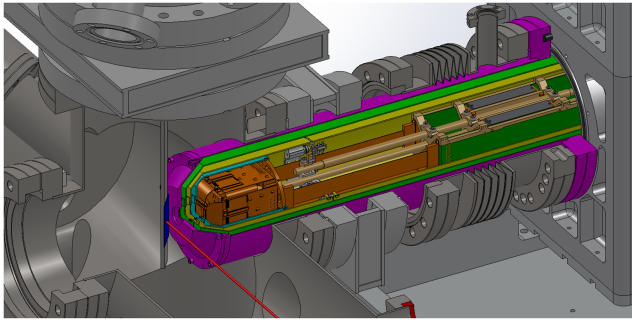


FIG. 5. CAD rendering of the detector protrusion of the NSLS-U7A TES spectrometer, with sample chamber, bellows, and radiation shields quarter-sectioned. *Purple*: Stainless-steel vacuum shield with 6 in. conflat flange (equivalent to DN100) to mate to the sample chamber. The vacuum shield is entrant through a bellows and 6 in. gate valve into the sample chamber; it has a total length of 34.7 cm from cryostat wall to its tip. A commercial, 1-atmosphere, grid-supported-polymer vacuum window separates the vacuum of the sample chamber from the vacuum of the spectrometer's cryogenic system. *Green*: Mu-metal shield of temperature 50 K with Al radiation window. *Yellow*: Mu-metal shield of temperature 3 K with Al radiation window. *Aqua*: Al shield of temperature 65 mK with Al radiation window. *Orange*: 65 mK snout detector package. When the spectrometer's vacuum window is at the minimum safe distance (as shown here) from the sample (*blue*; interrogated by X-ray beam, *red*), the distance from the beam spot on the sample to the TES array is 2.0 cm.

sample chamber; each spectrometer is designed to allow the detector protrusion to be brought to the center of its chamber. The minimum safe observing distance from sample to TES array is 2.0 cm. The other five deployed spectrometers are designed for hard X-rays, and their samples can thus be illuminated and observed in air. These five spectrometers share the design of the detector protrusion, which has a total length of 12.5 cm from cryostat wall to its tip. Again, the minimum safe sample distance from the TES array is 2.0 cm, but in all five measurement systems this sample distance is chosen to be larger. The vacuum-window flange has a bulkhead

mount for a KF-40 flange to allow the option of in-vacuum observations.

## H. Collecting efficiency

The chief advantage of a TES-array X-ray spectrometer over more traditional WD spectrometers is its collecting efficiency. In this section, we define collecting efficiency and give a pair of example calculations. Our definition assumes that X-rays are emitted isotropically, as in the case of, e.g., fluorescent emission. Thus, the following calculation is not directly applicable to measurements, such as directional scattering or those that employ a focusing-X-ray optic, in which the TES array is not evenly illuminated.

In the limit of a faraway source, the total collecting efficiency (CE) of a TES array is given by

$$CE(E) = QE(E) \cdot T(E) \cdot \Omega_{4\pi} \cdot N_{\text{pixels}}, \quad (6)$$

where  $QE(E)$  is the *quantum efficiency* or the fraction of X-rays (of a given energy) that are detected out of the total number that impinge upon the active area of the detector (see Table I);  $T(E)$  is the total transmission fraction (at a given energy) through all windows (see Table III);  $\Omega_{4\pi}$  is the solid angle subtended by each TES's aperture as viewed from the sample and expressed as a fraction of  $4\pi$  sr; and  $N_{\text{pixels}}$  is the total number of operating TESs in the array. CE( $E$ ) measures the fraction of the total emission from the sample that is captured by the TES array. For realistic sample distances (Table IV) and aperture-chip thicknesses (Sec. II C), CE( $E$ ) may be a few percent smaller than calculated via Eq. (6) due to shadowing by the aperture of divergent X-ray paths.

As examples, we calculate the collecting efficiency of the NSLS-U7A spectrometer at the O  $K\alpha$  line in its two intended science modes: PFY (partial-fluorescence-yield)-NEXAFS (near-edge X-ray absorption, fine structure) and XES (see Sec. IV D). This spectrometer has a hybrid TES array

TABLE IV. Summary of characteristics of the seven deployed spectrometer systems. Array and pixel types refer to entries in Table I.  $C \times R$  and  $t_{\text{row}}$  are the number of columns and rows and the row time in the time-division-multiplexed readout (see Sec. II D). Aperture-chip thickness is described in Sec. II C. A sample calculation of total collecting efficiency, based on the sample distance and other system parameters, is given in Sec. II H. No sample distance is listed for the NIST TR system; this system employs a focusing, polycapillary X-ray optic, so the efficiency calculation developed in Sec. II H does not apply. O'Neil *et al.*<sup>26</sup> discuss the properties of the optic and how they contribute to the overall collecting efficiency.

Spectrometer	Technique(s)	$E$ (keV) of expts.	Date deployed	Array type	Pixel types (No. of pixels)	TDM $C \times R$	$t_{\text{row}}$ (ns)	Aperture-chip thickness	Sample dist. (cm)
A. Lund Kemicentrum	TR-XAS; TR-XES	2–10	October 2010	ar13	7b (24)	$4 \times 6$	640	Full	20
			December 2013	ar13	7b (80); 9b (80)	$8 \times 20$	320	Full	4–20
B. NIST TR	TR-XAS; TR-XES	2–10	January 2013	ar13	8b (80); 9b (80)	$8 \times 20$	640	Full	...
			January 2015	ar14	8b(240)	$8 \times 30$	320	Full	...
C. NIST metrology	XRF line metrology	2–10	November 2012	ar13	8b (80); 9b (80)	$8 \times 20$	640	Full	13
D. NSLS beamline U7A (NIST)	PFY-NEXAFS; XES	0.25–1	October 2011	ar13	7b (60)	$3 \times 20$	640	Full	$\geq 2$
			April 2014	ar14	3b(120); 8b(120)	$8 \times 30$	320	Thinned	$\geq 2$
E. APS 29-ID	RSXS	0.25–1	Jul., 2014	ar14	3b(240)	$8 \times 30$	320	Thinned	$\geq 5$
F. Jyväskylä Pelletron	PIXE	1–14	February, 2011	ar13	8b (12)	$2 \times 6$	640	Full	30
			February 2014	ar13	8b (80); 9b (80)	$8 \times 20$	320	Full	15
G. PSI $\pi$ M1	$\pi^-$ -atom spectroscopy	4–15	October 2014	ar14	8b(240)	$8 \times 30$	320	Full	4–8

(Fig. 2(d)) of 120 large and 120 small TESs. The per-pixel solid-angle fraction is calculated from the aperture (Table I) and the sample distance (Table IV). In PFY-NEXAFS mode, all TESs can be used (although the efficiency is dominated by the larger TESs); in this case,  $CE(E) = 6.1 \times 10^{-4}$  at 525 eV (O  $K\alpha$ ). In XES mode, only the 120 small TESs have sufficient energy resolution to be used, so  $CE(E) = 5.0 \times 10^{-5}$ , which is nearly two orders of magnitude higher than for a high-efficiency grating spectrometer.<sup>15,22</sup>

More subtle advantages of TES-array spectrometers over WD technologies arise because WD spectrometers depend on geometry for their spectral resolving power while TES arrays, like energy-dispersive detectors generally, do not. To achieve high energy resolution, a WD spectrometer must either observe a small excitation spot on the sample (which can lead to rapid sample damage) or employ a restrictive entrance slit or collimate via Soller slits (either of which reduces flux and thus increases observation time and so can contribute to sample damage). By contrast, the TES can observe directly with no degradation in spectroscopic performance a sample illuminated by a de-focused spot that is as large as the sample itself. In addition, the TES observing geometry can be very flexible. Our two deployed synchrotron spectrometers and the Lund spectrometer can be moved quickly to any sample distance greater than the minimum. This means that in scattering experiments, the operator can adjust the angular coverage of a single TES (and the angular spacing between TESs) in real time to optimize measurement of a given angular scattering profile. In other measurements with more isotropic emission patterns, the sample distance can be adjusted to optimize the X-ray flux on the TESs.

## I. Energy resolution

Sec. II B and its accompanying Table I discuss the intrinsic (with non-multiplexed readout and at low count rates of a few counts/s/pixel) energy resolution of our present TESs. These values do not represent any inherent limit on the energy resolution of X-ray-TESs; rather, they are based on engineering choices related to the available cryogenic systems (Sec. II F). In Sec. VI A, we discuss the improved performance that we expect will be enabled by more capable cryogenics in future spectrometers.

In our deployed spectrometers, both higher multiplexing factors and elevated count rates can degrade energy resolution. While the mechanisms (see Sec. VI C) that cause this are common across spectrometers, the detailed effects are spectrometer- and application-specific. In the subsections of Sec. IV, we give the available measurements of the energy resolution achieved by each spectrometer under operating conditions that are relevant to its intended measurement applications. In future work, we intend to map these effects further. Sec. VI C details our ongoing engineering efforts to improve the readout so that full arrays can achieve the intrinsic energy resolution at high count rates.

## III. CREATION OF X-RAY SPECTRA FROM RAW DATA

The process of turning raw data streams from the various TESs in the array into an energy-calibrated X-ray spectrum

has two parts. First, a spectrum is produced for each TES via linear *optimal filtering* that is high-resolution but is not energy-calibrated. Second, each of these spectra is energy-calibrated. In most (but not all) measurements, this second step includes combination of the separate spectra into one. At the end of this process the experimenter retains, for each individual X-ray event, not only the X-ray energy but also knowledge of which TES pixel received the X-ray and the arrival time to as good as<sup>32</sup> 1.2  $\mu$ s (FWHM (full-width-at-half-maximum)). Positional information is used in scattering measurements (see Sec. IV E) and may be useful for future imaging applications. Timing information is combined with beamline-trigger information to reject background counts in the hadronic-atom experiments (Sec. IV G). Timing is also used in the time-resolved-spectroscopy measurements (Secs. IV A and IV B) to sort events into classes of pumped-sample, unpumped-sample, or calibration X-rays.

### A. Constrained optimal filtering

The electronics that support the TDM readout (Sec. II D) produce a data stream for each TES that represents TES current vs. time and is sampled at either  $f_{\text{samp}} = 156.25$  kHz (20-row deployed systems) or  $f_{\text{samp}} = 104.17$  kHz (30-row). A data-acquisition computer examines these time series to identify the onset of photon pulses. When a trigger condition is satisfied, the computer creates a *pulse record* consisting of samples both before and after the pulse arrival and stores it to disk for later analysis. The spectrometer operator can select the number of samples to record. Generally, longer records offer improved energy resolution<sup>60</sup> at the expense of reduced counting capability, as records that contain more than one pulse cannot be analyzed by the standard methods. In a typical configuration, records last 5–10 ms with one-quarter of the samples before the photon arrival.

Pulses from X-rays of different energies are extremely similar in shape, apart from noise. They differ primarily in pulse magnitude or *pulse height*. The usual analysis approach, then, is to estimate one pulse height from each record. Pulse records are modeled as a linear combination of a few terms, whose amplitudes are to be estimated in the presence of correlated (non-white), Gaussian noise. In most cases, the model contains only two terms: a standard pulse shape (measured via averaging of many pulses) and a constant offset. The offset term is needed because the quantity of interest is the pulse height relative to this slowly varying baseline.

The linearity of the signal model and the Gaussianity of the noise model reduce the numerical problem to one of summing the samples with a specific set of weights. The use of statistically optimal weighting of the data to estimate the pulse height in the presence of noise and additional, fixed-signal terms is called *constrained optimal filtering*.<sup>61,62</sup> Optimal filters depend on and are constructed from the noise-autocorrelation function and the pulse-shape model; once computed, they can be applied to pulse records quickly. This weighting is statistically optimal under several assumptions that are known to be approximately but not exactly true, which are as follows: pulses are transient departures from a strictly constant baseline level; the noise is an additive, stationary,

multivariate, Gaussian process independent of the signal level; and all pulses at any energy are proportional to a single standard pulse shape. The practice of pulse processing to yield unbiased pulse heights, including the correction of small systematic errors that requires some care in most X-ray-pulse analyses, is discussed more fully by Fowler *et al.*<sup>55</sup>

The standard method of optimal filtering has been found to work very well in a wide variety of measurements, but the approach presents two major limitations. First, the standard method does not adapt to the fact that the X-ray pulse shape varies with energy. Analysis of pulse records by methods that accommodate an energy-dependent shape has been attempted.<sup>63–67</sup> Such methods typically require a larger set of “training data” than does optimal filtering, and they have yet to be shown to improve pulse-height estimation either by a large factor or over a broad range of measurements. The second major limitation of optimal filtering is that it requires “clean” pulses without additional pulses piled up in any of the records. This requirement means that the standard method cannot be used at high input X-ray rates without a steep penalty in either energy resolution, output rate, or both. Methods have been proposed that fit for multiple pulse heights in a single, extended data record.<sup>14,68,69</sup> Such methods have a higher computational cost than optimal filtering, but some version of them, probably in combination with the energy-dependent-shape methods, could enable the operation of future TES spectrometers at much higher X-ray rates than are presently possible.

## B. Energy calibration

Optimal filtering of individual pulse records produces a pulse-height estimation that is initially devoid of information about absolute energy. The complex physics of devices operated in the superconducting transition prevents computation of the absolute calibration of a TES based on fundamental device properties. Instead, calibration must proceed from the observation in the pulse-height spectrum of features that have accurately known energies.

For the hard-X-ray band of 2 keV–15 keV, which covers our time-resolved (Secs. IV A and IV B), accelerator-based (Secs. IV F and IV G), and line-metrology (Sec. IV C) spectrometers, our team has worked out a general calibration procedure that involves a ladder of anchor points of the K lines of  $3d$  transition metals that were previously measured with great accuracy by others.<sup>70,71</sup> The calibration ladder is observed simultaneously with the X-rays of scientific interest in order to correct for gain drifts that can be of order part-per-thousand (e.g., 6 eV at 6 keV) over an observation period of hours. A nonlinear calibration function from pulse height to energy,  $E = f(P)$ , is determined separately for each TES in the array. Ideally, this function is built from anchor points covering an energy range broader than the range of scientific interest. One must take care in fitting data to known line shapes, in order to avoid biased results. An accurate model of the energy-response function of the TES is required (a pure Gaussian response may be inadequate<sup>33,34</sup>). To minimize bias, fits should be maximum-likelihood fits that account for the Poisson distribution of counts in a histogram bin.<sup>72</sup>

The calibration points can be combined into calibration functions in many different ways. We have found the most reliable method to be the construction of *smoothing splines* from the data.<sup>73</sup> “Smoothing” means that the spline does not strictly interpolate the calibration points, which in turn reduces the danger that the calibration curve will over-fit the uncertain, detailed structure of the data. In the most thorough absolute-energy calibration of TES X-ray spectra to date, Fowler *et al.*<sup>34</sup> used the NIST-metrology spectrometer (Sec. IV C) to derive an energy scale, based on the K lines of high-purity foils of Ti, Cr, Mn, Fe, and Co, whose absolute accuracy over the 4.5 to 7 keV range was estimated to be 0.4 eV. The primary source of uncertainty was the natural curvature (or nonlinearity) of the TES  $E$  vs.  $P$  functions. Future experiments that may require even better absolute accuracy in their energy calibration could use TESs that have been redesigned to have a more linear response—possibly at the expense of some loss in energy resolution.

For the soft-X-ray band below 2 keV, which covers our two synchrotron-based spectrometers (Secs. IV D and IV E), our team has yet to work out a general procedure for energy calibration. To date, we have relied on observations of elastically scattered X-rays from the beamline monochromator. Over a narrow energy range, a linear energy scale can be assumed, while a broader range requires construction of a nonlinear function,  $E = f(P)$ , as above for hard X-rays. In the soft-X-ray band, it is less important to observe calibration X-rays at all times, as part-per-thousand gain drifts have a small effect; drift by 0.5 eV of a line near 500 eV in a spectrum with 1 eV FWHM resolution would have a small effect in most planned measurements. Thus, we have found that energy calibration can generally be performed at the start of a set of soft-X-ray measurements and then verified several hours later. Future calibration methods may rely on targets of well-characterized, stable compounds like highly ordered pyrolytic graphite (HOPG), iron oxides, or standard-reference glasses to provide a ladder of well-spaced K- and L-series anchor lines.

## IV. DEPLOYED SPECTROMETERS

The seven deployed spectrometer systems are listed in Table IV, which summarizes many of the important system parameters. In Subsections IV A–IV G, we describe each spectrometer, the measurement apparatus in which it is embedded, and the measurement technique(s) it enables.

### A. Lund Kemicentrum: Time-resolved spectroscopy

The TES spectrometer deployed to Lund University’s Kemicentrum (Lund, Sweden) operates in conjunction with an ultrafast, broadband, pulsed-X-ray source.<sup>17,74</sup> A near-infrared pulsed laser excites a photo-active sample with a pulse of duration  $\approx 60$  fs, and also generates a pulse of X-rays of somewhat longer duration that reaches the sample after a tunable time delay. X-rays are generated via the *bremstrahlung* process when the laser accelerates electrons from the edge of a water jet into the jet. The laser pulses at 1 kHz, meaning that measurements are repeated every 1 ms.

This *pump-probe* apparatus can be run in two measurement modes. In the first mode, time-resolved X-ray-absorption spectroscopy (TR-XAS), the broadband X-ray source shines through a thin sample and onto the TES spectrometer. The measurement at a given delay setting is repeated every 1 ms until sufficient statistics are achieved. By determining the ratio of the energy spectrum of the transmitted X-rays recorded by the TES spectrometer to the X-ray-energy spectrum of the bare source (fit to a TES measurement made without the sample), the experimenter creates an absorption spectrum. Because of the broadband nature of both the source and the spectrometer, all elements/edges are recorded simultaneously. Each relevant edge spectrum is then analyzed via the standard techniques of EXAFS<sup>75</sup> (extended X-ray absorption fine structure, which is sensitive to the coordination environment surrounding the element of interest) and/or XANES (X-ray absorption near-edge structure, which is sensitive to the chemical state of the unoccupied valence orbitals of the element of interest). The time delay between pump and probe is then changed, another XAS spectrum is created, and the post-pump time evolution of the sample is mapped. In the second mode, time-resolved X-ray-emission spectroscopy (TR-XES), the broadband source X-rays strike the sample and the TES spectrometer records fluorescent emission. All emission lines from the sample are recorded simultaneously. XES measurements are sensitive to occupied valence orbitals, and so provide complementary information to that gleaned from XAS measurements. As in TR-XAS, the spectrum acquired at each delay setting is an accumulation of spectra acquired every 1 ms, and the pump-probe delay is varied to map the time evolution of the sample. In both absorption and emission modes, the “pump” excitation can be disabled and X-ray timing ignored. Thus, the system can also be used to perform *static* (non-pumped) measurements.

The TES spectrometer was installed in October 2010, with a demonstration-scale detector package (24 sensors in a 4-column  $\times$  6-row TDM arrangement). During the first measurement campaign,<sup>23,76</sup> the energy resolution was assessed via measurement of Mn  $K\alpha$  X-rays (5.9 keV) emitted by an <sup>55</sup>Fe source. The spectrometer achieved energy resolution in a combined spectrum (of all pixels) of  $\Delta E_{\text{combined}} = 3.1$  eV with the laser off and 3.4 eV with the laser on. Electrical interference from the laser system’s Pockels cell, which has since been mitigated, caused the difference. The whole system was used to measure a static-EXAFS spectrum at the Fe  $K$  edge (7.1 keV) of ferrocene,  $\text{Fe}(\text{C}_5\text{H}_5)_2$ , which was chosen as a representative example of the class of metal-ligand molecules to be studied. The spectrometer acquired  $8.9 \times 10^6$  total output X-ray events over 14.1 h (175 counts/s, or cps). Subsequent EXAFS analysis recovered features that were consistent with synchrotron reference data. This was the first EXAFS analysis of a spectrum obtained via a broadband source and an energy-dispersive spectrometer. Previously, Mitsuya *et al.*<sup>77</sup> used a static, broadband X-ray source and a single TES detector to record transmission spectra of thin, metallic Ti and Co foils; these measurements detected the Ti and Co K absorption edges but did not have the signal-to-noise ratio needed to see any fine-structure features. The prototype Lund spectrometer was also used to measure a static XES spectrum<sup>22</sup>

of  $\text{Fe}_2\text{O}_3$ : the spectral data clearly exhibited a prominent  $K\beta'$  feature about 15 eV below the peak of the main  $K\beta_{1,3}$  line, which is a signature of a high-spin Fe complex (see, e.g., Vankó *et al.*<sup>78</sup>).

The full detector package (160 sensors; 8-column  $\times$  20-row TDM; Fig. 2(a)) was delivered in late 2013 and upgraded readout electronics were delivered in late 2014. The full system achieved a combined energy resolution of  $\Delta E_{\text{combined}} = 3.5$  eV, at 5.9 keV at the end of commissioning in February 2016. A campaign of measurements of time-resolved XAS and XES with this system is presently underway.

## B. NIST: Time-resolved spectroscopy

The TES spectrometer deployed to NIST (Boulder, Colorado, USA) for time-resolved spectroscopy is used in conjunction with a pulsed-laser X-ray source that operates on the same principles as the one described in Sec. IV A. Other than the following, the Lund and NIST systems are very similar and enable the same types of time-resolved measurements. The NIST laser source,<sup>24</sup> developed during 2013 and 2014, has a minimum laser-pulse duration of 35 fs and has higher average power than that of Lund. A commercial, polycapillary, X-ray optic focuses the pulsed-X-ray flux from the water jet to a spot size of 83  $\mu\text{m}$  (FWHM) at the sample. The X-ray path from the sample to the TES spectrometer goes through a ring-shaped target of a custom alloy of 3d transition metals. This ring target is excited by an X-ray tube source to provide X-rays for energy calibration (see Sec. III B).

The full source and a demonstration-scale detector package (160 sensors; 8-column  $\times$  20-row TDM) were used<sup>24</sup> to acquire a static-EXAFS spectrum of an ammonium-ferrioxalate solution in water. The ferrioxalate ion is of interest due to its use as an actinometer<sup>79</sup> and because it consumes oxygen in many environmental water systems.<sup>80</sup>

The full detector package (240 sensors; 8-column  $\times$  30-row TDM; Fig. 2(b)) was installed in January 2015, and has been used for a variety of absorption- and emission-spectroscopy measurements. Fig. 6 shows static XANES spectra (obtained in transmission mode as described in Sec. IV A) of several Fe-containing compounds. These measurements demonstrate that our TES spectrometer can indeed identify chemical states of Fe via their absorption spectra. In another proof-of-principle measurement,<sup>25</sup> the TES spectrometer measured static-XES spectra of  $\text{Fe}_2\text{O}_3$  and  $\text{FeS}_2$ , which are known to be high-spin and low-spin Fe compounds, respectively. As expected based on previous XES measurements<sup>78</sup> of high-spin and low-spin Fe compounds with higher-resolution crystal spectrometers, the TES-XES spectrum of  $\text{Fe}_2\text{O}_3$  was measurably different from  $\text{FeS}_2$  in the intensity ratio of  $K\alpha_1:K\alpha_2$ , and the  $\text{Fe}_2\text{O}_3$  TES-XES spectrum exhibited a prominent  $K\beta'$  feature about 15 eV below the peak of the main  $K\beta_{1,3}$  line. Calculations<sup>25</sup> based on these measurements showed that the NIST system would be able to perform meaningful pump-probe XES measurements to determine the spin state of Fe vs. time in photo-induced reactions. The energy resolution of the TES spectrometer (all 240 sensors’ data combined into a single spectrum) in this measurement mode was  $\Delta E_{\text{combined}} = 5.5$  eV at the Fe  $K\alpha$  line (6.4 keV).

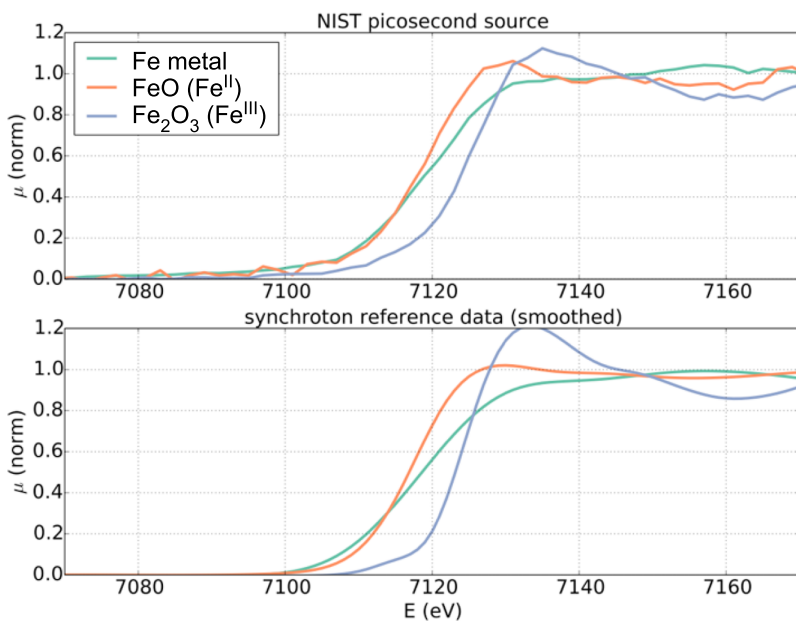


FIG. 6. XANES spectra (absorption length,  $\mu$ , normalized to have unity step-size at the Fe  $K$  edge, vs. energy) of three compounds that contain Fe in different oxidation states. *Upper*: Static (non-TR; excitation of samples disabled) transmission-mode XANES spectra acquired with the NIST broadband, water-jet, X-ray system, and 240-sensor TES spectrometer. The input count rate on TES spectrometer was about 4000 cps/array, and TES energy resolution was 9 eV in this measurement mode. A typical static-EXAFS spectrum is acquired in 4 h, during which approximately  $60 \times 10^6$  X-ray events are recorded and analyzed. Chemical shifts of the Fe edge are clearly observed. *Lower*: Synchrotron reference measurements<sup>81</sup> (XAFS Spectra Library: <http://cars.uchicago.edu/xaslib/search>) of the same compounds, smoothed to match the TES energy resolution. The TES-acquired spectra match the reference data.

The NIST system has also been used to perform two time-resolved-X-ray-spectroscopy measurements. In the first measurement of its type that did not employ a synchrotron or free-electron laser source, Miaja-Avila *et al.*<sup>27</sup> recorded the pump-probe TES-XES spectra of Fe tris bipyridine, an archetypal spin-crossover material, and measured the fraction of molecules in the excited, high-spin state via evolution of the measured Fe  $K\alpha$  and  $K\beta$  XES line shapes as a function of the delay between laser pump and X-ray probe. Via a fit to many delay settings, the lifetime of the high-spin (quintet) state was found to be described by an exponential decay of time constant  $570 \pm 100$  ps, which is consistent with previously published results. As part of this result, the temporal resolution of the entire NIST pump-probe system was calculated to be 2.5 ps and measured experimentally to be no larger than 6 ps. The energy resolution of the TES spectrometer in this measurement mode was  $\Delta E_{\text{combined}} = 5.2$  eV at 6.4 keV.

In the second time-resolved measurement, O'Neil *et al.*<sup>26</sup> compared the (unpumped) EXAFS spectrum of an ammonium-ferrioxalate aqueous solution, in which the central Fe atom of the ferrioxalate ion is known to be in the  $\text{Fe}^{\text{III}}$  state, to that acquired at a pump-probe delay of 100 ps (during the initial stage of the ferrioxalate photoreduction reaction). At 100 ps delay, the amplitude of the EXAFS features was reduced, and the Fe edge was shifted to lower energy by  $2.0 \pm 0.4$  eV, both of which are indicative of an intermediate  $\text{Fe}^{\text{II}}$  state. The measurement thus confirms a photoreduction model in which Fe is first reduced and then ligand bonds are cleaved. The steps involved in the photoreduction of ferrioxalate are not agreed upon in the literature.

### C. NIST: Metrology of X-ray lines and spectrometer development

The second TES spectrometer deployed to NIST/Boulder is intended primarily for *X-ray metrology*, or the measurement of X-ray fundamental parameters. This same spectrometer has also been used to investigate new multiplexing technologies

and new approaches to the analysis of X-ray data. For all of these measurements, the source is a commercial X-ray tube that fluoresces various metal targets. The TES array is of the ar13 type and has 160 sensors, half of which are 8-bars and half are 9-bars (Fig. 2(a)).

To date, the NIST X-ray metrology measurements have been of the widths, shapes, and central energies of the  $L$ -series emission lines of several metals from the lanthanide series. The characteristic-line energies of the X-ray radiation of each element are already tabulated,<sup>82</sup> however, many of the original data sets are at least fifty years old and suffer from systematic uncertainties that are difficult to estimate, and some line energies are altogether absent. The X-ray-analysis community has expressed a need for refined measurements of fundamental parameters.<sup>83</sup> We have begun a program to take advantage of the high sensitivity and wide simultaneous energy range of TESs in order to re-measure many of the less-well-established X-ray parameters. An important initial achievement was the establishment of an absolute-energy calibration for TESs accurate to better than 0.4 eV over the energy range of 4.5 keV–7 keV (see Sec. III for further discussion). During these initial measurements, the array was run at a relatively high X-ray photon rate of 15 cps per TES, and an older version of TDM readout was used that switched rows every 640 ns. With the high count rate and the slower readout, the energy resolution in the combined spectra was  $\Delta E_{\text{combined}} = 4.5$  eV at 6.4 keV.

This spectrometer was also used to reach the best energy resolution achieved via multiplexed readout of 32 TESs through a single amplifier chain. Via TDM readout (Sec. II D), the resolution was  $\langle \Delta E_{\text{FWHM}} \rangle = 2.55$  eV at 5.9 keV, averaged across all 32 channels.<sup>56</sup> The best sensor had energy resolution of 2.27 eV. The same TES array was also used to test a newer multiplexing architecture, code-division multiplexing (CDM). CDM is compatible with all existing TDM readout infrastructures and differs only in how the TESs are coupled to the multiplexing SQUIDS. Rather than reading out one TES at a time, CDM reads out all TESs at all times

with a set of positive and negative coupling polarities, and so offers a noise advantage over TDM because the wide-bandwidth SQUID-amplifier noise is not aliased severely into the TES signal band. A recent 32-channel CDM measurement<sup>49</sup> made in the NIST metrology spectrometer has achieved  $\langle \Delta E_{\text{FWHM}} \rangle = 2.77$  eV at 5.9 keV, with the best sensor achieving 2.28 eV.

Finally, the metrology spectrometer has been used to explore new approaches to the analysis of X-ray-pulse data. For example, Fowler *et al.*<sup>14</sup> studied the behavior of a single TES as the X-ray rate was increased to the point that current pulses frequently piled up on one another. This study tested a new technique for the simultaneous fit of multiple photon energies and showed one way to lessen the costly trade-off between the conflicting goals of high energy resolution and fast counting capability. Energy resolution achieved via this new method ranged from 2.12 eV at 6 keV at an input X-ray rate of 9 cps to 3.55 eV at 100 cps.

#### D. NSLS: Synchrotron absorption and emission spectroscopy

Our team's first synchrotron-based spectrometer is designed for two different measurement techniques: PFY-NEXAFS (defined below) and XES. In October 2011, the spectrometer was installed at beamline U7A of the National Synchrotron Light Source (NSLS; Brookhaven, New York, USA), a bending-magnet, soft-X-ray spectroscopy beamline run by NIST. The first array was of a demonstration scale of 60 TESs (3-column  $\times$  20-row TDM) of the ar13-7b (350  $\mu\text{m}$ —larger) device type. In April 2014, the full 240-pixel (8  $\times$  30 TDM; Figs. 1(e), 2(d), and 3(c)) detector array was installed. This array is unique among our spectrometers in that it is a “hybrid” of 120 of each of the two pixel sizes (larger—350  $\mu\text{m}$ ; smaller—124  $\mu\text{m}$ ). The full U7A spectrometer is shown in Fig. 4 and its mate to the U7A sample chamber is discussed in Fig. 5.

Near-edge X-ray absorption, fine structure<sup>84</sup> (NEXAFS) is the soft-X-ray analog of the XANES technique discussed in Secs. IV A and IV B. This widely used synchrotron technique probes the density of unoccupied valence orbitals. NEXAFS is commonly measured via total electron yield (TEY); this method requires only a low-noise ammeter to measure the current sourced by the sample to replace photoelectrons and Auger electrons ejected under X-ray illumination. An electron-energy analyzer enables the method of partial-electron-yield (PEY) NEXAFS to reject signals from atoms/edges that are not of interest. Both TEY-NEXAFS and PEY-NEXAFS are surface-sensitive. To look below the surface (e.g., to study buried interfaces in organic electronics or de-emphasize surface contamination in many types of samples) and/or to observe nonconductive samples, fluorescence yield can instead be used to measure NEXAFS absorption. As in electron-yield, there are total- (TFY) and partial-fluorescence-yield (PFY) methods. TFY-NEXAFS is simpler (any X-ray detector can be used) but can suffer from significant background contamination, especially in dilute samples and/or if the interrogating beam has significant harmonic content. PFY-NEXAFS requires an energy-resolving detector to window on the fluorescence line of interest.

The 120 larger pixels in our hybrid NSLS array are intended for PFY-NEXAFS measurements. These pixels provide a large collecting area while still achieving sufficient energy resolution of about 2.5 eV in the sub-keV soft-X-ray range (see Fig. 7). Figs. 8(a) and 8(b) show scatter plots of TES energy vs. beamline energy during a continuous scan of the C-K edge of a sample that contains 0.7% C by mass in a matrix of 20  $\mu\text{m}$  silica ( $\text{SiO}_2$ ) beads. Figs. 8(c) and 8(d) show a C-K edge PFY-NEXAFS measurement of the same sample. This would be a challenging sample to measure at the C-K edge via traditional total-yield NEXAFS methods—its non-conducting nature would defeat TEY-NEXAFS, and the

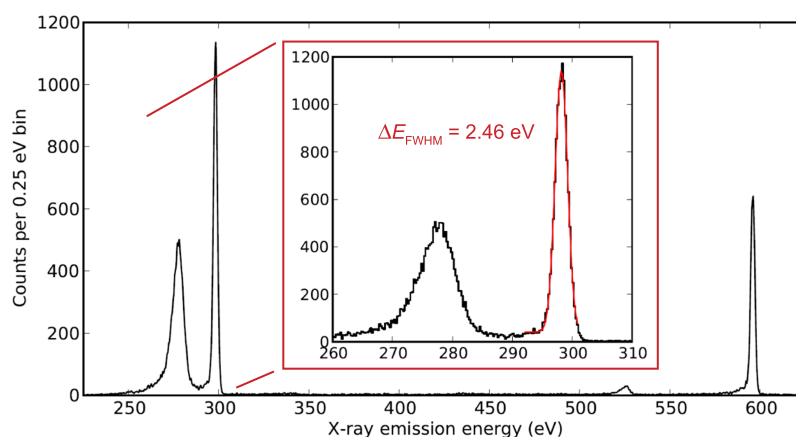


FIG. 7. TES-acquired elastic-scattering spectrum from a thin layer of gold plated on polished silicon, illuminated by a 297.8 eV monochromatic beam (plus harmonics) at NSLS-U7A. *Main plot*: From left to right, spectroscopic features are carbon  $K\alpha$  emission (275 eV) from organics adsorbed on the sample from air, the scattered beam (297.8 eV), oxygen  $K\alpha$  emission (525 eV) from adsorbed organics, and the second-order beam (595.6 eV). The spectrum is combined from a 3-column  $\times$  20-row TDM array of 350  $\mu\text{m}$  detectors of type ar13-7b. The scattering signal evenly illuminated the TES array due to the surface roughness of the gold. *Inset*: Enlarged view of the low-energy region of the spectrum. Histogrammed data are in black, while the fit to the scattered beam is in red. The fitted energy resolution is  $\Delta E_{\text{combined}} = 2.46 \pm 0.02$  eV at 297.8 eV. A similar fit (not shown) to the second-order beam gives  $\Delta E_{\text{combined}} = 2.54 \pm 0.03$  eV at 595.6 eV. Energy resolution of 2.5 eV is more than sufficient in most PFY-NEXAFS measurements to resolve the soft-X-ray K or L emission line of interest from the background of other K and L lines and the elastically scattered beam.

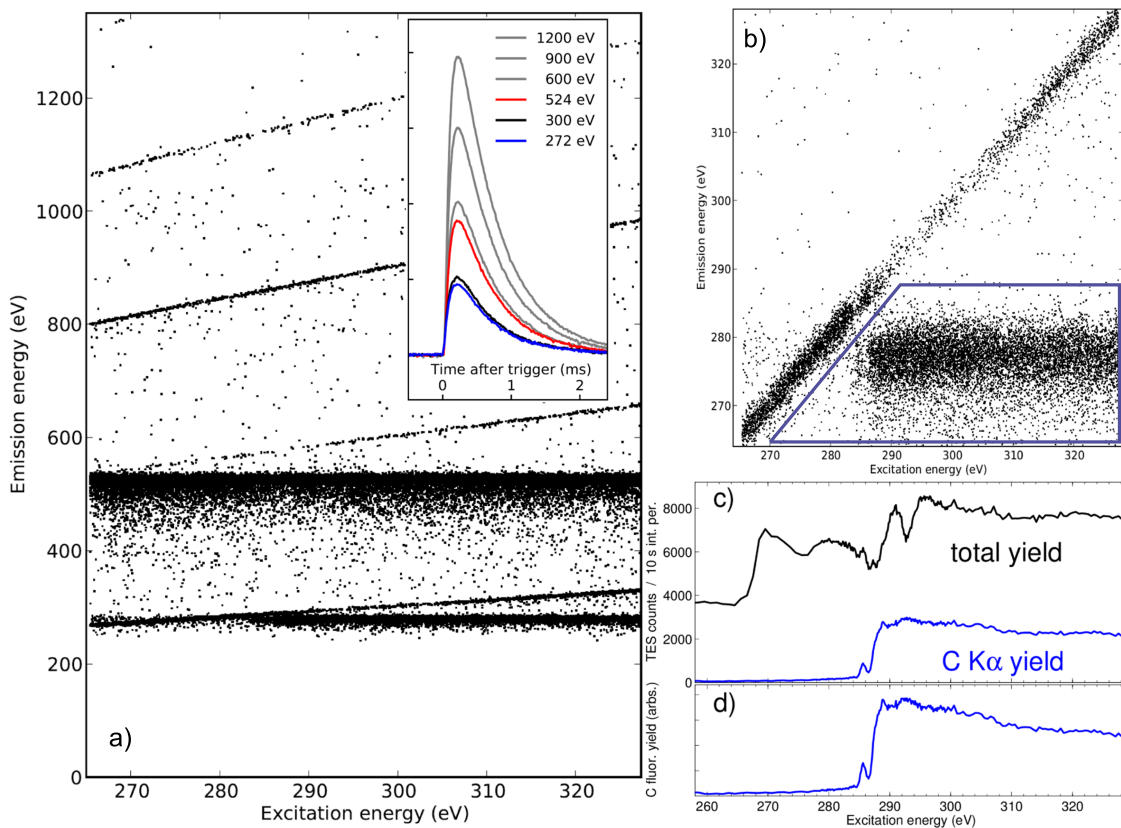


FIG. 8. C K edge scan ((a) and (b)) and C K PFY-NEXAFS spectrum ((c) and (d)), each recorded by the NSLS-U7A TES spectrometer. The sample in both measurements, NIST Standard Reference Material 1216-I, contains C in an unknown chemical state at 0.7% by mass in a matrix of porous micro-particulate silica beads of diameter  $\approx 20 \mu\text{m}$ . (a) Emission energy measured by the TES spectrometer (all energies measured simultaneously) vs. beam energy during a continuous beam scan from 266 eV to 328 eV at 0.2 eV/s. Each dot represents an X-ray. With an average ring current of 600 mA and monochromator entrance and exit slits of  $50 \mu\text{m}$ , the bending-magnet beamline produced an average of about  $8 \times 10^{10}$  photons/s. Each  $350 \mu\text{m}$  TES saw an average count rate of 11 cps. The C K $\alpha$  signal is the horizontal band centered at 278 eV. Backgrounds include the elastically scattered beam (fundamental through fifth-order; thin diagonal bands) and O K $\alpha$  emission from the silica matrix (horizontal band centered at 530 eV; excited by harmonics; about 70% of the total counts). *Inset*: TES current (raw data; not filtered) vs. time in six individual X-ray-pulse records from the same TES, acquired at a beam energy of 300 eV. The pulses (smallest to largest) correspond to C K $\alpha$  fluorescence, first-order beam, O K $\alpha$  fluorescence, second-order beam, third-order beam, and fourth-order beam. (b) The same data as in (a), with the TES energy scale zoomed to show C K fluorescent emission and the elastically scattered fundamental. The *blue* box shows the region within which events should be counted as C K $\alpha$  signal X-rays in a PFY-NEXAFS scan. The larger TESs have energy resolution of  $\Delta E_{\text{combined}} \approx 2.5$  eV across the 200 eV–1400 eV band, and thus easily resolve the signal from all components of the background. (c) Total counts (upper trace, *black*) and C K $\alpha$  counts (lower trace, *blue*) recorded by the one hundred and twenty  $350 \mu\text{m}$  TESs in each 10 s integration period. Here the monochromator was scanned in a mode more optimized for NEXAFS, with 1 eV steps from 258 eV to 278 eV, 0.15 eV steps from 278 eV to 299 eV, and 0.5 eV steps from 299 eV to 328 eV. The full scan took 38 min, during which the TES array recorded  $1.8 \times 10^6$  counts. Monochromator slits were again  $50 \mu\text{m}$  each, and the average ring current was 450 mA. The total-yield absorption spectrum shows significant features that are due to background contamination, including the sharp rise at 268 eV that is caused by excitation of the O K edge by the second-order beam (536 eV). The C-yield spectrum has high signal-to-noise ratio and is virtually background-free. (d) C K-edge PFY NEXAFS spectrum: the C K $\alpha$  spectrum from (c) divided by the beam intensity.

large O content that is excited by beamline harmonics would create large backgrounds in TFY-NEXAFS (Fig. 8(c); upper trace).

A different kind of low-temperature detector, the superconducting tunnel-junction (STJ), has also found a niche in synchrotron-based PFY-NEXAFS measurements,<sup>85,86</sup> and so provides a useful comparison to our work here. The STJ is not a microcalorimeter, but instead works on a principle very similar to that of a SDD or other solid-state detector: pair breaking. In a STJ, the absorbed X-ray breaks Cooper pairs of electrons to create its signal voltage instead of electron-hole pairs as in a SDD. Because the gap is much smaller (meV-scale in STJs vs. a few eV in SDDs), the number of pairs created is several orders of magnitude higher and the energy resolution, which scales as  $E/\Delta E \propto \sqrt{N_{\text{pairs}}} \propto 1/\sqrt{\Delta_{\text{gap}}}$  (assuming similar Fano factors<sup>87</sup> of around 0.1), is much better. STJs can also

generally count faster than most existing X-ray TESs<sup>88</sup> because their decay mechanism is electronic rather than thermal. STJ elements are roughly the same size as TESs. They have been built into arrays of the scale of one hundred detectors,<sup>88,89</sup> but the lack of a practical multiplexed-readout scheme means that future scaling beyond kilopixel arrays is anticipated to be more difficult for STJs than for TESs. Present STJ-based spectrometers employ real-time signal processing, while TES spectrometers are still being advanced toward that goal. While STJs have sufficient energy resolution to window on fluorescence lines in most soft-X-ray PFY-NEXAFS measurements and are well suited to this technique, they have not yet been applied to our second TES soft-X-ray-synchrotron application, XES, due to insufficient energy resolution. Although energy resolution better than 3 eV FWHM has been achieved in STJs for

X-ray energies below 400 eV,<sup>90,91</sup> resolution of 5 eV–15 eV is more typical<sup>86,88</sup> in this energy range and energy resolution degrades at higher energies as  $\sqrt{E}$  due to Fano statistics.

The second technique enabled by the TES spectrometer at NSLS-U7A is soft-X-ray XES. XES, as discussed for hard X-rays in Sec. IV B, probes occupied valence orbitals to study, e.g., the spin state, coordination environment, or oxidation state of a sample. Our team used the demonstration-scale array of 60 larger TESs to record nitrogen XES spectra<sup>14,22</sup> of ammonium nitrate ( $\text{NH}_4\text{NO}_3$ ) and the explosive RDX (also known as hexogen or cyclotrimethylenetrinitramine;  $\text{C}_3\text{H}_6\text{N}_6\text{O}_6$ ), two compounds that contain nitrogen in different and well-defined chemical states. In acquisition times of 29 min ( $\text{NH}_4\text{NO}_3$ ) and 23 min (RDX), our measurements achieved similar signal-to-noise ratio as those performed by Vila *et al.*<sup>92</sup> in 30 min each with a traditional grating-based emission spectrometer at an undulator beamline ( $\approx 10^3$  times U7A's beam flux). Although the larger TESs ( $\Delta E_{\text{combined}} = 2.5$  eV) were able to resolve many emission-spectral features, soft-X-ray XES generally requires resolution closer to 1 eV to resolve eV-scale shifts in line positions and changes in line shapes that are due to chemistry. The 120 smaller pixels in our hybrid NSLS array, with an intrinsic energy resolution of about 1.1 eV (Fig. 9), are intended for XES.

The NSLS was decommissioned in September 2014. NIST is commissioning new beamlines at Brookhaven's NSLS-II. A new TES spectrometer (see Sec. V) is under development for NSLS-II beamline 7-ID-1, with delivery planned for late 2017.

### E. APS: Resonant soft-X-ray scattering (RSXS)

Resonant soft-X-ray scattering (RSXS) is a leading technique<sup>29,93</sup> to probe valence-band ordering in exotic electronic

materials, such as the cuprate superconductors, in which the valence electrons are thought to self-organize into spatially heterogeneous phases, such as stripe phases.<sup>28,29,94,95</sup> In RSXS, the incident energy of the monochromatic X-ray beam is tuned, on-resonance, to excite core-shell electrons into unoccupied valence states in the material under study. The probability of electronic transition into the valence band depends strongly on the spin, charge, and orbital configurations of the valence electrons. The excited electron recombines with a core hole and decays back to the ground state and an X-ray of the same energy as the incident one is re-emitted (or *elastically scattered*). This resonance occurs at precise scattering angles determined by the spatial geometry of the valence electrons. RSXS measures the scattering intensity as functions of both angle and excitation energy, and so simultaneously probes the *spatial ordering* and *energetics* of the valence-electronic states.

In most RSXS experiments, the scattered X-rays are measured by an energy-integrating, imaging, area detector such as a CCD camera or a micro-channel plate. A major difficulty is that RSXS scans generate an enormous background of incoherent, inelastic x-ray fluorescence, the generation of which is unavoidable and inherent to the RSXS technique. This fluorescence background can be overcome in RSXS studies of a subset of materials and dopant concentrations: those that have long-range, highly ordered electronic states, so the scattering peak has a sharp enough angular distribution to be resolvable above the background with sufficient statistics in long integration times. Even in these ideal systems, the peak scattering signal is typically a small fraction of the background and can be less than a few percent above the background (e.g., da Silva Neto *et al.*<sup>95</sup>). However, in many interesting materials, the long-range electronic ordering is hypothesized to transition into a glassy (short-range order, long-range disorder) phase as the doping is increased (e.g., Smadici *et al.*<sup>96</sup>), so the RSXS scattering signal would become more diffuse in angle and thus blend even further into the fluorescence background. To date, RSXS performed with an energy-integrating detector has been unable to determine whether electronic charge ordering enters this glassy phase or disappears altogether.

An alternate approach in RSXS is to use a spectroscopic detector to resolve (and thus separate) the scattering signal from the fluorescence background. For this purpose, our team installed a TES spectrometer in July 2014 on the new RSXS endstation at beamline 29-ID (IEX-CDT<sup>97</sup>) of the Advanced Photon Source (APS; Argonne, Illinois, USA). The spectrometer mates to a large (1.1 m-diameter) UHV sample chamber which is designed to contain a UHV-compatible kappa-geometry diffractometer with a cryogenic sample stage. The spectrometer's 240-sensor array of 3-bars TESs (8-column  $\times$  30-row TDM; Fig. 2(c)) is optimized for performance in the soft-X-ray band below 2 keV. The detector protrusion is the most extreme of any our team has developed so far: it extends 0.95 m from the exterior wall of the cryostat. It mates to the sample chamber via an 8 in. conflat flange and vacuum bellows and allows the TES array to reach the center of the large sample chamber. The detector spans a range of scattering angles about a fixed center of  $125^\circ$ , which is the angle at which scattering from glassy electronic order in cuprates is believed to

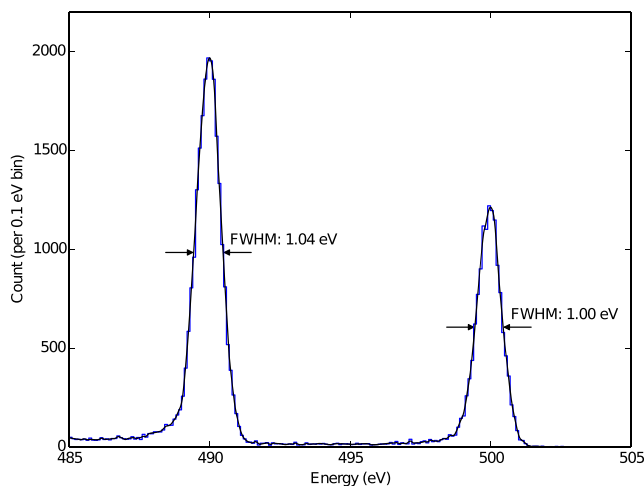


FIG. 9. TES-acquired elastic-scattering spectrum showing specular reflection from a Ce:YAG crystal when illuminated by 490 eV and then 500 eV monochromatic X-rays at APS-29ID. The *black* trace shows histogrammed data, while the *blue* trace is the fit spectrum. The array was run in an 8-column  $\times$  4-row TDM arrangement. While 32 TESs were being read out during the measurement, the highly directional scattering signal illuminated only a single TES. Here, the TES energy calibration assumes linear response between 490 and 500 eV. The achieved energy resolution is  $\Delta E_{\text{FWHM}} = 1.0$  eV at 500 eV, which will be sufficient to separate the elastic-scattering signal from most of the fluorescence background in general RSXS measurements.

be most intense. At the spectrometer's closest approach to the sample that does not block the beam, the distance from the TES array to the sample is 5 cm. To demonstrate the performance of the spectrometer, we observed, in specular reflection, elastic scattering from a Ce-doped  $\text{Y}_3\text{Al}_5\text{O}_{12}$  (Ce:YAG) crystal (Fig. 9). The achieved energy resolution was  $\Delta E_{\text{FWHM}} = 1.0$  eV at 500 eV.

A high-efficiency grating spectrometer<sup>15,98</sup> can be used as the spectroscopic receiver in RSXS experiments. Ghiringhelli *et al.*<sup>94</sup> used this approach to study a cuprate superconductor with a long-range electronic order. Although this measurement had very high energy resolution (combined resolution of spectrometer and beamline monochromator of 0.13 eV at the 930 eV Cu  $L_3$  edge during this experiment), the spectra showed a peak separation between the elastic-scattering signal and the d-d exciton background of  $\approx 2$  eV, and thus indicated that resolution of  $\Delta E_{\text{FWHM}} \approx 1$  eV should be sufficient to eliminate most of the d-d exciton and Cu L-fluorescence backgrounds. The total collecting efficiency (CE; Sec. II H) in the sub-keV band of a high-efficiency grating spectrometer<sup>15</sup> is roughly the same as that of a *single sensor* in our 240-sensor spectrometer at APS-29ID. The TES array thus allows simultaneous, high-efficiency measurements of 240 independent scattering solid-angles spanning a maximum of  $10.3^\circ$  in each direction.

Beamline 29-ID entered its commissioning phase in June 2014. The first RSXS science measurements were begun by our team in late 2016, and are ongoing.

## F. Jyväskylä Pelletron: Particle-induced X-ray emission spectroscopy

Particle-induced X-ray-emission (PIXE) spectroscopy uses ion-beam excitation to determine the elemental composition of a sample. Our team has deployed a spectrometer to the PIXE beamline of Jyväskylä's Pelletron accelerator facility (Jyväskylä, Finland). The beamline produces a focused, 2 MeV proton beam of spot size 2 mm.

PIXE has several advantages<sup>31</sup> over more standard techniques that use electron-beam excitation, such as SEM-EDS (scanning-electron microscope excites the sample and energy-dispersive X-ray spectroscopy is performed via a SDD). The proton beam induces a much smaller *bremsstrahlung* background signal, which can be the sensitivity limiter in electron-excited spectroscopy. Also, a proton beam is more penetrating than an electron beam, so PIXE probes bulk (sub-surface) composition. Finally, PIXE does not require the sample to be in vacuum, meaning large and/or delicate samples, such as paintings and biological samples, can be analyzed.

PIXE is traditionally performed with a SDD spectrometer. A TES spectrometer's energy resolution gives it two advantages over a SDD ( $\Delta E_{\text{FWHM}} \approx 125$  eV at 6 keV) which increase sensitivity to trace elements in PIXE: the ability to resolve almost all elemental line-overlaps and better peak-to-background ratios. Crystal spectrometers, which have energy resolution that is comparable to or better than that of TES spectrometers, generally do not have the collection efficiency to allow PIXE spectra to be acquired in reasonable times.

The PIXE-TES spectrometer was installed in February 2011, with a demonstration-scale detector package (12 sensors; 2-column  $\times$  6-row TDM). The energy resolution of the Jyväskylä spectrometer was determined via measurement<sup>31</sup> of Mn  $K\alpha$  X-rays (5.9 keV) from an<sup>55</sup> Fe source. The spectrometer achieved average (across all pixels) energy resolution of  $\langle \Delta E_{\text{FWHM}} \rangle = 3.8$  eV. Palosaari *et al.*<sup>31</sup> used the demonstration-scale spectrometer to conduct initial PIXE observations of a bulk-metal Mn sample. In contrast to the Mn spectrum produced by the<sup>55</sup> Fe source, the PIXE Mn spectrum showed a dim satellite peak about 25 eV above the main Mn  $K\alpha_{1,2}$  complex. This is interpreted to be a multivacancy feature (see, e.g., Jun<sup>99</sup>) caused by the simultaneous ejection of two core electrons, and provides an interesting example of a spectral-emission feature whose visibility is significantly aided by the energy resolution, collecting efficiency, and wide simultaneous spectral coverage of the TES spectrometer.

The full detector package (160 sensors; 8-column  $\times$  20-row TDM; Fig. 2(a)) and upgraded readout electronics were deployed in early 2014. Palosaari *et al.*<sup>30</sup> undertook a commissioning campaign to assess detection limits of trace elements in PIXE-TES; samples included standard-reference materials and various paint pigments. A highlight of the campaign was the observation of eV-scale chemical shifts in the Ti  $K\alpha$  and  $K\beta$  complexes in samples known to contain Ti in different oxidation states. Thus, the PIXE-TES system at Jyväskylä can be used to study the chemical (in addition to elemental) composition of samples.

## G. PSI: Spectroscopy of pionic atoms

A hadronic atom is an atom in which an electron has been replaced by a negatively charged hadron, such as a pion ( $\pi^-$ ) or anti-kaon ( $K^-$ ). Because the hadron is much more massive than the electron it replaces, the electronic transition energies are shifted to higher energies by an amount that is sensitive to the hadron's mass. For instance, the 4–3 transitions of pionic carbon ( $\pi^-^{12}\text{C}$ ) generate 6.4 keV X-rays.<sup>33</sup> A hadronic atom is created when a beam of non-relativistic hadrons is directed at a target that contains the atoms of interest. The hadronic atom forms in a highly excited electronic state and decays through a cascade of transitions into less excited states via X-ray and Auger emission. At the end of the cascade, the atomic nucleus absorbs the hadron. The binding energies and resulting X-ray-line energies can be calculated via quantum-mechanical methods in which a purely electromagnetic Hamiltonian is perturbed by the interaction between the hadron and nucleus due to the strong force. The strong-force perturbation produces eV-scale shifts in the energies of some inner-shell X-ray transitions and also broadens these lines.<sup>100</sup> Thus, high-resolution X-ray spectra from hadronic atoms can be used to study the strong nuclear force. The eventual goal of the multi-institutional HEATES (High-resolution Exotic Atom x-ray spectroscopy with Transition-Edge Sensors) collaboration is to study the interaction between the anti-kaon and various atomic nuclei via TES-based X-ray spectroscopy. The family of kaons, or  $K$  mesons, are the lightest (and thus most straightforward to produce) hadrons to contain a strange quark or antiquark.

To test the operation of a TES spectrometer in the environment of a hadron beamline, the HEATES team deployed a TES spectrometer to the  $\pi$ M1 beamline of the Paul Scherrer Institute's Laboratory for Particle Physics (Villigen, Switzerland) for a three-week experimental campaign during October and November of 2014. The spectrometer consisted of 240 of the 8-bars, ar14 pixels in an 8-column  $\times$  30-row TDM arrangement (Fig. 2(b)). The pion beam was stopped in a hollow, conical, carbon target to create, primarily,  $\pi^{-12}\text{C}$ . An X-ray tube source excited a secondary target, visible through a hole in the main carbon target, of high-purity chromium and cobalt foils to create a ladder of their K lines for energy calibration. The tube source also excited, more dimly, lines of iron from stainless-steel fittings around the apparatus. With the pion beam off, the spectrometer achieved combined energy resolution<sup>32</sup> of  $\Delta E_{\text{combined}} = 4.6$  eV at 6.4 keV (Fe  $K\alpha$ ) at an input count rate of 4.4 cps/pixel. With the pion beam on, the achieved resolution was  $\Delta E_{\text{combined}} = 6.8$  eV at 6.4 keV. The difference was due to deposition of energy in the bulk silicon of the TES-array chip by charged particles from the beam, which in turn creates thermal-crosstalk pulses.<sup>33</sup>

Highlights of the measurement campaign included:<sup>32</sup> simultaneous observation of the ( $\pi^{-12}\text{C}$ ) lines near 6.43 keV due to the parallel  $4f-3d$  and  $4d-3p$  transitions, whose centroids are only 7 eV apart; absolute-energy calibration to 0.12 eV ( $1-\sigma$ , quadrature combination of statistical and systematic uncertainties) over a narrow energy band around the Fe  $K\alpha$  lines at 6.4 keV; and integration of beamline and spectrometer triggers with timing resolution of 1.2  $\mu\text{s}$  (FWHM). These measurements verify that a TES spectrometer can achieve the energy resolution, energy calibration, timing resolution, and sensitivity required for the planned kaon measurements. A new TES spectrometer<sup>101</sup> (see Sec. V) is under development to measure kaonic atoms at beamline K1.8BR of the Japan Proton Accelerator Research Complex (J-PARC; Tokai, Japan) in early 2018.

## V. PLANNED SPECTROMETERS

Five more spectrometers are presently under development. All have the same architecture as the seven spectrometers already deployed. The only difference is that they will use the newer generation of TDM readout (described in Secs. II D and VI C) that switches rows twice as fast and has half the amplifier noise,<sup>56</sup> which will enable improved energy resolution. Table V summarizes many of the planned system parameters.

Two of our planned spectrometers are for the techniques of soft-X-ray emission and absorption spectroscopy discussed in Sec. IV D. The first was deployed to beamline 10-1 of the Stanford Synchrotron Light Source (SSRL; Menlo Park, CA, USA) in February 2016, and is presently undergoing commissioning. The second is under development as a user instrument for NSLS-II beamline 7-ID-1 and is planned to be deployed in late 2017.

The third new spectrometer is for the technique of kaonic-atom spectroscopy discussed in Sec. IV G. It underwent a first set of commissioning measurements<sup>101</sup> in the beam environment of kaon beamline K1.8BR of the Japan Proton Accelerator Research Complex (J-PARC; Tokai, Japan) in June 2016. The HEATES collaboration is presently applying for beam time at K1.8BR to measure spectra of kaonic atoms.

The final two planned spectrometers are to be deployed to electron-beam-ion-trap (EBIT) facilities. An EBIT uses a strong and focused electron beam to create and contain highly ionized atoms. Such ionized states occur naturally in various types of astrophysical plasmas. One of these spectrometers, under a project led by the microcalorimeter group at NASA's Goddard Spaceflight Center and nicknamed TEMS<sup>35</sup> (Transition-edge EBIT Microcalorimeter Spectrometer), is planned for the EBIT at Lawrence Livermore National Laboratory (LLNL; Livermore, CA, USA). The TEMS will supplement the existing EBIT Calorimeter Spectrometer, or ECS, which is a 36-sensor array of silicon-thermistor microcalorimeters,<sup>103,104</sup> to measure emission spectra of astrophysically relevant processes such as charge exchange<sup>35</sup> between ions and neutral species. The TES array<sup>102</sup> for TEMS has 256 TESs with close-packed, overhanging absorbers. The TEMS spectrometer is intended to be deployed to the LNLL EBIT in 2017. The other of these two spectrometers is planned for the EBIT at NIST (Gaithersburg, MD, USA). The NIST-EBIT spectrometer is intended to measure emission spectra from highly charged, mid-to-high-Z ions to test modern atomic theory and quantum-electrodynamic effects, among other applications. Deployment of the NIST-EBIT spectrometer is planned to be in early 2018.

## VI. FUTURE IMPROVEMENTS

While TES-microcalorimeter spectrometers have improved dramatically in recent years, continued development is both desirable and likely. In this section, we discuss

TABLE V. Summary of characteristics of the five planned spectrometer systems. Array and pixel types refer to entries in Table I.  $C \times R$  and  $t_{\text{row}}$  are the planned number of columns and rows and the row time in the time-division-multiplexed readout (see Sec. II D). Aperture chips of different thicknesses are described in Sec. II C. The LLNL EBIT system will use a detector array<sup>102</sup> fabricated by the detector group at NASA's Goddard Spaceflight Center; these detectors have close-packed absorbers and thus do not require individual apertures over each TES.

System	Technique(s)	$E$ range of expts.	Array type	Pixel types (No. of pixels)	TDM $C \times R$	$t_{\text{row}}$ (ns)	Aperture-chip thickness
SSRL 10-1	PFY-NEXAFS; XES	250 eV–1 keV	ar14	3b (240)	$8 \times 30$	160	Thinned
J-PARC K1.8BR	$K^-$ -atom spectroscopy	5 keV–7 keV	ar14	8b (240)	$8 \times 30$	160	Full
LLNL TEMS	EBIT	50 eV–10 keV	NASA	NASA (256)	$8 \times 32$	160	none
NSLS-II 7-ID	PFY-NEXAFS; XES	250 eV–1 keV	ar14	3b(120); 8b(120)	$8 \times 30$	160	Thinned
NIST EBIT	EBIT	250 eV–10 keV	ar14	8b (240)	$8 \times 30$	160	Full

anticipated improvements to the detectors, the multiplexed readout, and the cryogenics that will expand the capabilities of future spectrometer arrays.

### A. Operation at lower temperatures

Our present generation of spectrometers relies on a commercial cryogenic platform (Sec. II F) that provides robust, reliable, and cryogen-free cooling to a steady bath temperature of 65 mK, which is well-matched to our present TES-operating temperature of  $T_{\text{op}} = 107 \text{ mK}–108 \text{ mK}$ . New cryogenic systems, including pulse-tube-backed, cryogen-free versions of both dilution refrigerators and  $^3\text{He}$ -backed ADRs, can provide in a practical package stable bath temperatures as low as 10 mK–30 mK with sufficient cooling power to maintain those temperatures with the expected loads from TES arrays of up to  $\approx 10\,000$  pixels. This colder range of bath temperatures will allow TES-operating temperatures of  $T_{\text{op}} \approx 55 \text{ mK}$ , or a factor of two lower than in our present spectrometers, within a couple of years. Lower  $T_{\text{op}}$  will, in turn, allow improved energy resolution and increased per-pixel collecting area.

The dynamic range of a TES microcalorimeter scales as  $E_{\text{max}} \propto CT_{\text{op}}/\alpha_I$  (Eq. (5)). Reduction of  $T_{\text{op}}$  by a factor of two while  $E_{\text{max}}$  is maintained requires the ratio  $C/\alpha_I$  to double. Whether this is accomplished via a doubling of  $C$  or a halving of  $\alpha_I$  or some combination of the two, the energy resolution improves by a net factor of  $\sqrt{2}$  (Eq. (4)). In the hard-X-ray regime, the performance of our present ar13-7b devices (Table I) indicates that  $\Delta E = 1.7 \text{ eV}$  at 6 keV should be feasible at  $T_{\text{op}} \approx 55 \text{ mK}$ . For soft X-rays, an ar14-3b device whose  $C$  per unit area is that of the ar13 devices (see discussion in Sec. II B) that is then scaled to  $T_{\text{op}} \approx 55 \text{ mK}$  as above should achieve  $\Delta E = 0.6 \text{ eV}$  at 500 eV. Other paths to additional improvement in energy resolution are active areas of research in the TES field, and include further reductions in “unexplained noise”<sup>43</sup> and operation in a regime of much higher  $\beta_I$  so that lower values of  $C$  can be used.<sup>12</sup>

A lower operating temperature will also allow sensors with increased collecting area. In this cryogenic temperature range, the specific heat of the materials that contribute to  $C$  scales as  $c_V(T) \propto T_{\text{op}}$ . Therefore, if  $T_{\text{op}}$  is halved, the volume of the contributing materials needs to double to maintain  $C$ , and to increase by a factor of 2–4 to maintain  $E_{\text{max}}$ . A straightforward way to achieve this would be to keep all material thicknesses approximately constant and increase the area of the TES by a factor of 2–4. Thus, the linear size of a future soft-X-ray TES with  $T_{\text{op}} \approx 55 \text{ mK}$  would grow by a factor of between  $\sqrt{2}$  and 2 (from the present 124  $\mu\text{m}$  to the range of 175  $\mu\text{m}$ –248  $\mu\text{m}$ ). Similarly, a future hard-X-ray, low- $T_{\text{op}}$  TES would grow in linear size from 350  $\mu\text{m}$  to the range of 495  $\mu\text{m}$ –700  $\mu\text{m}$ .

Unless corrected for, a lower operating temperature would also affect the TES’s thermal-decay time constant, which scales as  $\tau_{\text{TES}} \propto C/(G\alpha_I)$  in the limit of strong electrothermal feedback. Thermal conductance scales with the TES’s linear size ( $L_{\text{TES}}$ ) and temperature as  $G \propto L_{\text{TES}}T_{\text{op}}^{n-1}$ ; typical values of the unitless constant  $n$  are between 3 and 4 for thin  $\text{SiN}_x$  in this temperature range.<sup>105</sup> Thus, reduction of  $T_{\text{op}}$  to 55 mK and the corresponding increase in the linear dimension to

maintain  $E_{\text{max}}$  would decrease the thermal conductance to the bath to a factor of between 0.18 and 0.50 of the 107 mK value, which would in turn increase  $\tau_{\text{TES}}$  by a factor of between 4 and 11.3. To maintain counting capability, it is desirable to maintain  $\tau_{\text{TES}}$  and thus  $G$ . Fortunately, Hays-Wehle *et al.*<sup>106</sup> have demonstrated the ability to increase  $G$  controllably by more than two orders of magnitude via addition of normal-metal features on the  $\text{SiN}_x$  membrane, so we are confident that we can increase  $G$  to maintain the same  $\tau_{\text{TES}}$  even at lower  $T_{\text{op}}$ .

In summary, we expect the next generation of cryogenic systems to enable TES X-ray spectrometers with roughly 1.4 times the resolving power and two to four times the collecting area of our present spectrometers, while maintaining the present counting capability.

### B. Reduction in low-energy tailing

The X-ray absorber on each of our present-generation TESs is a 2.5  $\mu\text{m}$ –4.1  $\mu\text{m}$ -thick layer of evaporated Bi (see Sec. II B). We have discovered that the evaporated Bi distorts the energy-response function of the TESs to give a one-sided exponential tail to lower energies (see, e.g., Fig. 9). To account for this effect, spectra acquired with these sensors must be analyzed<sup>34</sup> via a Bortels function,<sup>107</sup> which is the convolution of a Gaussian with a single-sided exponential and a delta function. The physical mechanism that causes this low-energy tail is an active area of research, but we speculate that some fraction of the X-ray energy absorbed in the Bi resides in an energy state with a thermal decay time that is much longer than  $\tau_{\text{TES}}$ . Potential energy-loss paths include metastable electronic states or movements of atomic cores within the Bi lattice. We observe that the fraction of the total energy in this tail component increases both with X-ray energy and with Bi thickness. Typically,<sup>33</sup> 10%–30% of the energy resides in this tail component and the exponential-decay constant is tens of eV. This tail component, when properly accounted for in the energy-response function, is a minor nuisance during data processing and spectral analysis.

Low-energy tails are not fundamental to TES microcalorimeters nor even to Bi absorbers, and we expect that this feature will be eliminated in future arrays. Recently, we have tested devices with all-Au absorbers, and found no evidence of this low-energy-tail component. These devices provide comparable collecting area and quantum efficiency and achieve (Gaussian) energy resolution that is similar to that of our Bi-absorber devices. Further, the microcalorimeter group at NASA/GSFC has demonstrated tail-free spectra in devices where the Bi was electroplated (instead of evaporated) on Au to create a composite Bi/Au absorber.<sup>108</sup> Finally, we are collaborating with the Detector Group at Argonne National Laboratory to study the effects of Bi grain size on low-energy tailing and to compare directly the characteristic of Bi absorbers deposited via various methods.<sup>109</sup>

### C. Near-term improvements to TDM readout

The modest degradation in energy resolution with  $N_{\text{rows}}$  in our TDM readout is due to aliasing of amplifier noise.<sup>48,52</sup> In our deployed hard-X-ray spectrometers, the size of this effect

approaches 1.0 eV with 30 TDM rows. Because the number of TDM rows to be read out can be adjusted straightforwardly and in real time, the spectrometer operator can reduce the number of detectors per readout column (and thus increase proportionally the acquisition time required for a given number of total counts in a spectrum) when a specific measurement demands better energy resolution than is achievable with full-array readout. However, we consider this to be a temporary remedy, and the near-term goal is that the full array produces spectra with the best energy resolution. A newer version of our TDM-readout system<sup>56</sup> that will be used in the five near-future spectrometers has amplifier noise that is reduced by a factor of two, so the effect of this source of signal degradation is reduced to about 0.2 eV even in 32-row TDM readout. In addition, development of even quieter TDM readout continues, and improved readout circuitry will be integrated into existing spectrometers as it becomes available. Finally, the drop-in-compatible code-division<sup>49</sup> (CDM) scheme discussed in Sec. IV C offers a near-term route to significant reduction in amplifier noise via a significant reduction in the aliasing factor.

The degradation in energy resolution with X-ray flux is caused by electrical crosstalk between sensors. The strongest crosstalk source is inductive coupling among various elements within the TDM circuitry. Crosstalk is generally more important at higher energies, because the crosstalk signal and its subsequent contribution to energy resolution are proportional to the X-ray energy while the (undegraded) energy resolution scales as the square root of the X-ray energy. For instance, the two spectrometers deployed for soft-X-ray measurements, NSLS-U7A (Sec. IV D) and APS-29-ID (Sec. IV E) see very little degradation in resolution with X-ray flux up to 20 cps/pixel. In many of our present hard-X-ray measurement applications that are photon-starved, the effect of crosstalk on energy resolution is already small. Generally, the experimenter can decrease the X-ray flux (e.g., by increasing the sample distance to the detector array) in order to balance the energy resolution with the acquisition time required to perform a given measurement. However, when the NIST time-resolved system (Sec. IV B) is run in transmission-detected XAS mode, the energy resolution can degrade to about 10 eV at 7 keV (which is sufficient to resolve EXAFS features) for several reasons. In this mode this spectrometer routinely receives X-rays at count rates of greater than 5000 cps/array (>20 cps/pixel). Furthermore, a significant fraction of this flux is above 10 keV, which is well above the desired signal band but contributes heavily to crosstalk. Finally, the X-rays generated by the laser and water jet arrive nearly simultaneously, which means the crosstalk signals are concurrent with the signal X-rays, and so shift the derived X-ray energies by the maximum amount. Engineering efforts are underway to mitigate inductive crosstalk in future TDM circuits. In the near term, it should be possible to boost the per-pixel count rates at which the best energy resolution is possible from a few cps to 100 cps or more.

TES arrays beyond the 240–256-pixel scale are already under development. The European Space Agency, with contributions from NASA, is planning to launch the ATHENA satellite in the late 2020s with a 4000 pixel microcalorimeter

array.<sup>110</sup> To prepare for ATHENA, NIST and NASA's Goddard Space Flight Center are co-developing a spectrometer with 960 sensors arranged in a 24-column  $\times$  40-row configuration. This system will be compatible with both TDM and CDM readout; its completion is anticipated in late 2017. TES spectrometers at the kilopixel or even several kilopixel scale are also under active discussion for various terrestrial applications.

#### D. Faster detectors

Faster individual sensors can increase the spectrometer's maximum total count rate. The fundamental expression for the energy resolution of a TES microcalorimeter has no explicit dependence on the sensor speed or the thermal conductance to the bath ( $G$ ), the parameter that is most easily adjusted to make sensors faster.<sup>41</sup> Thus, there is no fundamental conflict between sensor speed and energy resolution. However, faster sensors often operate at higher  $I_{op}/I_{c0}$  ( $I_{c0}$  is the critical current of the superconducting film at zero temperature). This, in turn, suppresses<sup>111,112</sup>  $\alpha_I$  (defined in Eq. (2)) which makes the achievement of excellent energy resolution more challenging because resolution scales as  $1/\sqrt{\alpha_I}$  (Eq. (4)). Nonetheless, a variety of work<sup>106,113</sup> suggests that the thermal  $1/e$  recovery times of future sensors will be near or even below 100  $\mu$ s, rather than hundreds of microseconds as is common now. These faster recovery times are compatible with per-pixel count rates near 1000 cps. Due to the high current-slew rates of their pulses, these faster detectors are not compatible with 30-row TDM readout, even after the improvements in the newer version described in Sec. VI C. Thus, new multiplexing techniques are needed.

#### E. Multiplexed readout beyond TDM and CDM

Advanced multiplexing technologies are under development that will enable significantly faster TESs, significantly larger arrays, or both.

There are many reasons to push significantly beyond the present size scale of TES X-ray arrays. Arrays of 160–256 pixels are too small for most imaging applications. In addition, while the resolving power of microcalorimeter X-ray sensors is roughly two orders of magnitude better than that of conventional semiconducting sensors, the maximum count rate of a single SDD can be two orders of magnitude higher than that of a 240 element microcalorimeter array. The maximum total count rate a TES array can process is directly proportional to the number of sensors. Higher instrumental count rates are particularly desirable for materials-analysis applications where elevated x-ray fluxes are already encountered. Finally, photon-starved applications will benefit from the larger collection area of arrays with more elements.

Modern microfabrication techniques make the construction of silicon chips containing multi-kilopixel quantities of sensors or readout circuitry straightforward. However, integration of sensors with readout circuits beyond the kilopixel scale is a significant challenge that will need to be addressed in the future. For example, to expand our present spectrometer architecture (TES sensors on a central silicon chip, ringed by additional chips containing the readout circuitry) to 5000

sensors, the central silicon “chip” would need to have diameter of more than 300 mm in order to provide enough perimeter for 5000 pairs of wire bond pads on a 200  $\mu\text{m}$  pair pitch; the active area of the TES array itself would be only about 40 mm on a side. A variety of approaches can overcome this geometric challenge but many require more sophisticated fabrication techniques than are presently used such as combining sensors and readout on the same silicon substrate or the use of more demanding interconnects such as indium bump bonds. It is anticipated that a variety of approaches will be successfully pursued.

Larger arrays and faster sensors will strain existing readout techniques. The analog bandwidth and dynamic-range density available in single TDM or CDM columns are not expected to improve by the amounts needed. Fortunately, microwave-SQUID readout appears likely to provide the required advance in capabilities.<sup>50,114,115</sup> In microwave-SQUID readout, the current through each sensor is inductively coupled to a rf-SQUID. Each rf-SQUID is embedded in a thin-film resonant circuit, such that a change in flux in that rf-SQUID shifts the resonant frequency of the corresponding resonator. All resonant circuits are coupled to a common feed line and the response of the sensors is probed via a sum of microwave tones. The combined signals are amplified by a single, high-bandwidth, cryogenic, semiconductor amplifier. Microwave-SQUID readout can be thought of as increasing the readout bandwidth per amplifier column from the roughly 10 MHz of TDM and CDM to several GHz. This increase in bandwidth enables higher multiplexing factors and/or the measurement of faster sensors. Recent experiments at NIST have already achieved a single-column analog bandwidth of 1 GHz and a multiplexing factor of greater than 100.

## VII. CONCLUSION

TES arrays are an emerging technology for X-ray spectroscopy. Our team has deployed seven of these spectrometers. The flexibility and collecting efficiency of TES spectrometers have enabled new measurements and techniques at beamlines, in laboratory systems, and at accelerators across a variety of scientific fields. Another five spectrometers of this type are presently under development. As the technology continues to improve, we anticipate that advances in energy resolution, sensor speed, and array size will make future generations of TES-microcalorimeter X-ray spectrometers ever more capable.

## ACKNOWLEDGMENTS

The NIST/Boulder authors acknowledge support from the NIST Innovations in Measurement Science program, the NASA APRA and SAT programs, and the DOE Office of Basic Energy Sciences. L.M.-A., K.M.M., and G.C.O. were supported by National Research Council Post-Doctoral Fellowships.

Lund: The authors acknowledge long-term technical support from Villy Sundström and Wilfred Fullagar and the rest of the Lund team including Alireza Honarfar, Ujjwal Mandal, Dharmalingam Kurunthu, Fredrik Parnefjord Gustafsson, Amal El Nahas, Pavel Chabera, and Torbjörn

Pascher. We acknowledge support from the ERC Advanced Investigator Grant No. 226136, Crafoordska stiftelsen, the faculty of Science at Lund University, the Lund Laser Center, and the Marie Curie early research training program by the European Commission. J.U. acknowledges continued funding from the Knut and Alice Wallenberg Foundation.

APS: P.A. and Y.F. acknowledge support from DOE Grant No. DE-FG02-06ER46285. The construction of the IEX beamline was supported in part by National Science Foundation under Grant No. DMR-0703406. Work at Argonne National Laboratory is supported by the U.S. Department of Energy, Office of Science, under Contract No. DE-AC02-06CH11357.

Jyvaskylä: The authors thank the group of Ilari Maasilta for installing and using the PIXE spectrometer.

PSI and J-PARC: The authors thank many members of the HEATES collaboration, especially Dr. Shinji Okada, Dr. Shinya Yamada, and Dr. Tadashi Hashimoto, for preparing and executing the experiments at PSI beamline  $\pi\text{M1}$  and the preliminary experiments at J-PARC beamline K1.8BR. We also thank the technical and facilities teams at  $\pi\text{M1}$  led by Konrad Deiters and the technical and facilities teams at J-PARC for enabling our beam times to run so smoothly. We acknowledge support from Grants-in-Aid for Scientific Research from MEXT and JSPS (Nos. 25105514, 26707014, 24105003, 15H05438, 15H00785, 16K17718, and 16H02190), the Incentive Research Grant from RIKEN, and the Mitsubishi Foundation (26145). H.T. acknowledges support from the strategic young researcher overseas visits program for accelerating brain circulation by JSPS (No. R2509).

SSRL: The authors thank the SLAC team, including Dennis Nordlund, Jamie Titus, Sang Jun Lee, Ron Marks, Jason Knight, Dale Li, and Kent Irwin, for their roles in installing and exercising the spectrometer at SSRL beamline 10-1.

EBIT: The authors thank Scott Porter and Steve Smith of NASA/GSFC for technical discussions regarding the TEMS spectrometer for LLNL and Yuri Ralchenko of NIST for technical discussions regarding the NIST EBIT.

Certain commercial equipment and materials are identified in this paper in order to adequately specify the construction of the spectrometers. Such identification does not imply recommendation or endorsement by the National Institute of Standards and Technology, nor does it imply that the materials or equipment identified is necessarily the best available for the purpose. This work is a contribution of an agency of the United States Government; content not subject to copyright.

<sup>1</sup>D. H. Smith, G. Gillett, M. P. de Almeida, C. Branciard, A. Fedrizzi, T. J. Weinholt, A. Lita, B. Calkins, T. Gerrits, H. M. Wiseman, S. W. Nam, and A. G. White, *Nat. Commun.* **3**, 625 (2012).

<sup>2</sup>D. A. Bennett, R. D. Horansky, D. R. Schmidt, A. S. Hoover, R. Winkler, B. K. Alpert, J. A. Beall, W. B. Doriese, J. W. Fowler, C. P. Fitzgerald, G. C. Hilton, K. D. Irwin, V. Kotsubo, J. A. B. Mates, G. C. O’Neil, M. W. Rabin, C. D. Reintsema, F. J. Schima, D. S. Swetz, L. R. Vale, and J. N. Ullom, *Rev. Sci. Instrum.* **83**, 093113 (2012).

<sup>3</sup>S. Hatakeyama, M. Ohno, H. Takahashi, R. M. T. Damayanthi, C. Otani, T. Yasumune, T. Ohnishi, K. Takasaki, and S. Koyama, *J. Low Temp. Phys.* **176**, 560 (2014).

<sup>4</sup>M. Croce, M. Bacrania, E. Bond, D. Dry, W. A. Moody, M. Rabin, D. Bennett, G. Hilton, R. Horansky, V. Kotsubo, D. Schmidt, J. Ullom, L. Vale, and R. Cantor, *J. Low Temp. Phys.* **167**, 955 (2012).

- <sup>5</sup>L. Gastaldo, K. Blaum, A. Doerr, C. E. Düllmann, K. Eberhardt, S. Eliseev, C. Enss, A. Faessler, A. Fleischmann, S. Kempf, M. Krivovuchenko, S. Lahiri, M. Maiti, Y. N. Novikov, P. C.-O. Ranitzsch, F. Simkovic, Z. Szusc, and M. Wegner, *J. Low Temp. Phys.* **176**, 876 (2014).
- <sup>6</sup>B. Alpert, M. Balata, D. Bennett, M. Biasotti, C. Boragno, C. Brofferio, V. Ceriale, D. Corsini, P. K. Day, M. De Gerone, R. Dressler, M. Faverzani, E. Ferri, J. Fowler, F. Gatti, A. Giachero, J. Hays-Wehle, S. Heinitz, G. Hilton, U. Köster, M. Lusignoli, M. Maino, J. Mates, S. Nisi, R. Nizzolo, A. Nucciotti, G. Pessina, G. Pizzigoni, A. Puiu, S. Ragazzi, C. Reintsema, M. R. Gomes, D. Schmidt, D. Schumann, M. Sisti, D. Swetz, F. Terranova, and J. Ullom, *Eur. Phys. J. C* **75**, 112 (2015).
- <sup>7</sup>M. P. Croce, M. W. Rabin, V. Mocko, G. J. Kunde, E. R. Birnbaum, E. M. Bond, J. W. Engle, A. S. Hoover, F. M. Nortier, A. D. Pollington, W. A. Taylor, N. R. Weiss-Bernstein, L. E. Wolfsberg, J. P. Hays-Wehle, D. R. Schmidt, D. S. Swetz, J. N. Ullom, T. E. Barnhart, and R. J. Nickles, *J. Low Temp. Phys.* **184**, 958 (2016).
- <sup>8</sup>S. Kempf, A. Ferring, A. Fleischmann, M. Wegner, and C. Enss, *J. Low Temp. Phys.* **184**, 344 (2015).
- <sup>9</sup>S. R. Bandler, J. S. Adams, J. Beyer, W.-T. Hsieh, R. L. Kelley, C. A. Kilbourne, J.-P. Porst, F. S. Porter, H. Rotzinger, G. M. Seidel, S. J. Smith, and T. R. Stevenson, *AIP Conf. Proc.* **1185**, 579–582 (2009).
- <sup>10</sup>Hitomi Collaboration (215 co-authors), *Nature* **535**, 117 (2016).
- <sup>11</sup>J. N. Ullom and D. A. Bennett, *Supercond. Sci. Technol.* **28**, 084003 (2015).
- <sup>12</sup>S. J. Smith, J. S. Adams, C. N. Bailey, S. R. Bandler, J. A. Chervenak, M. E. Eckart, F. M. Finkbeiner, R. L. Kelley, C. A. Kilbourne, F. S. Porter, and J. E. Sadleir, *J. Low Temp. Phys.* **167**, 168 (2012).
- <sup>13</sup>S. J. Lee, J. S. Adams, S. R. Bandler, J. A. Chervenak, M. E. Eckart, F. M. Finkbeiner, R. L. Kelley, C. A. Kilbourne, F. S. Porter, J. E. Sadleir, S. J. Smith, and E. J. Wassell, *Appl. Phys. Lett.* **107**, 223503 (2015).
- <sup>14</sup>J. W. Fowler, B. K. Alpert, W. B. Doriese, D. A. Fischer, C. Jaye, Y. I. Joe, G. C. O’Neil, D. S. Swetz, and J. N. Ullom, *Astrophys. J., Suppl. Ser.* **219**, 35 (2015).
- <sup>15</sup>O. Fuchs, L. Weinhardt, M. Blum, M. Weigand, E. Umbach, M. Bär, C. Heske, J. Denlinger, Y.-D. Chuang, W. McKinney, Z. Hussain, E. Gullikson, M. Jones, P. Batson, B. Nelles, and R. Follath, *Rev. Sci. Instrum.* **80**, 063103 (2009).
- <sup>16</sup>A. C. Hudson, W. C. Stolte, D. W. Lindle, and R. Guillemin, *Rev. Sci. Instrum.* **78**, 053101 (2007).
- <sup>17</sup>W. Fullagar, J. Uhlig, M. Walczak, S. Canton, and V. Sundström, *Rev. Sci. Instrum.* **79**, 103302 (2008).
- <sup>18</sup>R. Cantor and H. Naito, *Microsc. Microanal.* **20**, 1146 (2014).
- <sup>19</sup>H. Muramatsu, K. Nagayoshi, T. Hayashi, K. Sakai, R. Yamamoto, K. Mitsuda, N. Y. Yamasaki, K. Maehata, and T. Hara, *J. Low Temp. Phys.* **184**, 91 (2016).
- <sup>20</sup>K. Maehata, T. Hara, K. Mitsuda, M. Hidaka, K. Tanaka, and Y. Yamanaka, *J. Low Temp. Phys.* **184**, 5 (2016).
- <sup>21</sup>S. Friedrich, *J. Synchrotron Radiat.* **13**, 159 (2006).
- <sup>22</sup>J. Uhlig, W. B. Doriese, J. W. Fowler, D. S. Swetz, C. Jaye, D. A. Fischer, C. D. Reintsema, D. A. Bennett, L. R. Vale, U. Mandal, G. C. O’Neil, L. Miaja-Avila, Y. I. Joe, A. El Nahhas, W. Fullagar, F. Parnefjord Gustafsson, V. Sundström, D. Kurunthu, G. C. Hilton, D. R. Schmidt, and J. N. Ullom, *J. Synchrotron Radiat.* **22**, 766 (2015).
- <sup>23</sup>J. Uhlig, W. Fullagar, J. N. Ullom, W. B. Doriese, J. W. Fowler, D. S. Swetz, N. Gador, S. E. Canton, K. Kinnunen, I. J. Maasilta, C. D. Reintsema, D. A. Bennett, L. R. Vale, G. C. Hilton, K. D. Irwin, D. R. Schmidt, and V. Sundström, *Phys. Rev. Lett.* **110**, 138302 (2013).
- <sup>24</sup>L. Miaja-Avila, G. C. O’Neil, J. Uhlig, C. L. Cromer, M. L. Dowell, R. Jimenez, A. S. Hoover, K. L. Silverman, and J. N. Ullom, *Struct. Dyn.* **2**, 024301 (2015).
- <sup>25</sup>Y. I. Joe, G. C. O’Neil, L. Miaja-Avila, J. W. Fowler, R. Jimenez, K. L. Silverman, D. S. Swetz, and J. N. Ullom, *J. Phys. B: At., Mol. Opt. Phys.* **49**, 024003 (2016).
- <sup>26</sup>G. C. O’Neil, L. Miaja-Avila, Y. I. Joe, B. K. Alpert, M. Balasubramanian, D. M. Sagar, W. B. Doriese, J. W. Fowler, W. K. Fullagar, N. Chen, G. C. Hilton, R. Jimenez, B. Ravel, C. D. Reintsema, D. R. Schmidt, K. L. Silverman, D. S. Swetz, J. Uhlig, and J. N. Ullom, *J. Phys. Chem. Lett.* **8**, 1099 (2017).
- <sup>27</sup>L. Miaja-Avila, G. C. O’Neil, Y. I. Joe, B. K. Alpert, N. H. Damrauer, W. B. Doriese, S. M. Fatur, J. W. Fowler, G. C. Hilton, R. Jimenez, C. D. Reintsema, D. R. Schmidt, K. L. Silverman, D. S. Swetz, H. Tatsuno, and J. N. Ullom, *Phys. Rev. X* **6**, 031047 (2016).
- <sup>28</sup>P. Abbamonte, L. Venema, A. Rusydi, G. A. Sawatzky, G. Logvenov, and I. Bozovic, *Science* **297**, 581 (2002).
- <sup>29</sup>P. Abbamonte, A. Rusydi, S. Smadici, G. D. Gu, G. A. Sawatzky, and D. L. Feng, *Nat. Phys.* **1**, 155 (2005).
- <sup>30</sup>M. R. J. Palosaari, M. Käyhkö, K. M. Kinnunen, M. Laitinen, J. Julin, J. Malm, T. Sajavaara, W. B. Doriese, J. Fowler, C. Reintsema, D. Swetz, D. Schmidt, J. N. Ullom, and I. J. Maasilta, *Phys. Rev. Appl.* **6**, 024002 (2016).
- <sup>31</sup>M. R. J. Palosaari, K. M. Kinnunen, J. Julin, M. Laitinen, M. Napari, T. Sajavaara, W. B. Doriese, J. Fowler, C. Reintsema, D. Swetz, D. Schmidt, J. Ullom, and I. J. Maasilta, *J. Low Temp. Phys.* **176**, 285 (2014).
- <sup>32</sup>S. Okada, D. A. Bennett, C. Curceanu, W. B. Doriese, J. W. Fowler, J. D. Gard, F. P. Gustafsson, T. Hashimoto, R. S. Hayano, S. Hirenzaki, J. P. Hays-Wehle, G. C. Hilton, N. Ikeno, M. Iliescu, S. Ishimoto, K. Itahashi, M. Iwasaki, T. Koike, K. Kuwabara, Y. Ma, J. Marton, H. Noda, G. C. O’Neil, H. Outa, C. D. Reintsema, M. Sato, D. R. Schmidt, H. Shi, K. Suzuki, T. Suzuki, D. S. Swetz, H. Tatsuno, J. Uhlig, J. N. Ullom, E. Widmann, S. Yamada, J. Yamagata-Sekihara, and J. Zmeskal, *Prog. Theor. Exp. Phys.* **2016**, 091D01.
- <sup>33</sup>H. Tatsuno, W. B. Doriese, D. A. Bennett, C. Curceanu, J. W. Fowler, J. Gard, F. P. Gustafsson, T. Hashimoto, R. S. Hayano, J. P. Hays-Wehle, G. C. Hilton, M. Iliescu, S. Ishimoto, K. Itahashi, M. Iwasaki, K. Kuwabara, Y. Ma, J. Marton, H. Noda, G. C. O’Neil, S. Okada, H. Outa, C. D. Reintsema, M. Sato, D. R. Schmidt, H. Shi, K. Suzuki, T. Suzuki, J. Uhlig, J. N. Ullom, E. Widmann, S. Yamada, J. Zmeskal, and D. S. Swetz, *J. Low Temp. Phys.* **184**, 930 (2016).
- <sup>34</sup>J. W. Fowler, B. K. Alpert, D. A. Bennett, W. B. Doriese, J. D. Gard, G. C. Hilton, L. T. Hudson, Y.-I. Joe, K. M. Morgan, G. C. O’Neil, C. D. Reintsema, D. R. Schmidt, D. S. Swetz, C. I. Szabo, and J. N. Ullom, “A Reassessment of Absolute Energies of the X-ray L Lines of Lanthanide Metals,” *Metrologia*, (to be published); preprint [arXiv:1702.00507](https://arxiv.org/abs/1702.00507).
- <sup>35</sup>G. L. Betancourt-Martinez, J. Adams, S. Bandler, P. Beiersdorfer, G. Brown, J. Chervenak, R. Doriese, M. Eckart, K. Irwin, R. Kelley, C. Kilbourne, M. Leutenegger, F. S. Porter, C. Reintsema, S. Smith, and J. Ullom, *Proc. SPIE* **9144**, 91443U (2014).
- <sup>36</sup>J. D. Gillaspay, *Phys. Scr.* **89**, 114004 (2014).
- <sup>37</sup>K. D. Irwin, *Nucl. Instrum. Methods Phys. Res., Sect. A* **559**, 718 (2006).
- <sup>38</sup>J. E. Sadleir, S. J. Smith, I. K. Robinson, F. M. Finkbeiner, J. A. Chervenak, S. R. Bandler, M. E. Eckart, and C. A. Kilbourne, *Phys. Rev. B* **84**, 184502 (2011).
- <sup>39</sup>A. Kozorezov, A. A. Golubov, D. D. E. Martin, P. A. J. de Korte, M. A. Lindeman, R. A. Hijmering, J. van der Kuur, H. F. C. Hoevers, L. Gottardi, M. Y. Kupriyanov, and J. K. Wigmore, *Appl. Phys. Lett.* **99**, 063503 (2011).
- <sup>40</sup>D. A. Bennett, D. R. Schmidt, D. S. Swetz, and J. N. Ullom, *Appl. Phys. Lett.* **104**, 042602 (2014).
- <sup>41</sup>K. D. Irwin and G. C. Hilton, “Transition-edge sensors,” in *Cryogenic Particle Detection*, Topics in Applied Physics, Vol. 99, edited by C. Enss (Springer-Verlag, Berlin, 2005), pp. 63–150.
- <sup>42</sup>J. N. Ullom, J. A. Beall, W. B. Doriese, W. D. Duncan, L. Ferreira, G. C. Hilton, K. D. Irwin, C. D. Reintsema, and L. R. Vale, *Appl. Phys. Lett.* **87**, 194103 (2005).
- <sup>43</sup>J. N. Ullom, W. B. Doriese, G. C. Hilton, J. A. Beall, S. Deiker, W. D. Duncan, L. Ferreira, K. D. Irwin, C. D. Reintsema, and L. R. Vale, *Appl. Phys. Lett.* **84**, 4206 (2004).
- <sup>44</sup>D. S. Swetz, D. A. Bennett, K. D. Irwin, D. R. Schmidt, and J. N. Ullom, *Appl. Phys. Lett.* **101**, 242603 (2012).
- <sup>45</sup>J. M. Martinis, G. C. Hilton, K. D. Irwin, and D. A. Wollman, *Nucl. Instrum. Methods Phys. Res., Sect. A* **444**, 23 (2000).
- <sup>46</sup>H. K. Collan, M. Krusius, and G. R. Pickett, *Phys. Rev. B* **1**, 2888 (1970).
- <sup>47</sup>B. L. Henke, E. M. Gullikson, and J. C. Davis, *At. Data Nucl. Data Tables* **54**, 181 (1993).
- <sup>48</sup>W. B. Doriese, J. A. Beall, W. D. Duncan, L. Ferreira, G. C. Hilton, K. D. Irwin, C. D. Reintsema, J. N. Ullom, L. R. Vale, and Y. Xu, *Nucl. Instrum. Methods Phys. Res., Sect. A* **559**, 808 (2006).
- <sup>49</sup>K. M. Morgan, B. K. Alpert, D. A. Bennett, E. V. Denison, W. B. Doriese, J. W. Fowler, J. D. Gard, G. C. Hilton, K. D. Irwin, Y. I. Joe, G. C. O’Neil, C. D. Reintsema, D. R. Schmidt, J. N. Ullom, and D. S. Swetz, *Appl. Phys. Lett.* **109**, 112604 (2016).
- <sup>50</sup>J. A. B. Mates, G. C. Hilton, K. D. Irwin, L. R. Vale, and K. W. Lehnert, *Appl. Phys. Lett.* **92**, 023514 (2008).
- <sup>51</sup>H. Akamatsu, L. Gottardi, C. P. de Vries, J. S. Adams, S. R. Bandler, M. P. Bruijn, J. A. Chervenak, M. E. Eckart, F. M. Finkbeiner, J. R. Gao, J.-W. den Herder, R. den Hartog, H. Hoevers, R. E. Kelley, P. Khosropanah, C. A. Kilbourne, J. van der Kuur, S.-J. Lee, A. J. van den Linden, F. S. Porter,

- K. Ravensberg, J. E. Sadleir, S. J. Smith, T. Suzuki, E. J. Wassell, and M. Kiviranta, *J. Low Temp. Phys.* **184**, 436 (2016).
- <sup>52</sup>J. A. Chervenak, K. D. Irwin, E. N. Grossman, J. M. Martinis, C. D. Reintsema, and M. E. Huber, *Appl. Phys. Lett.* **74**, 4043 (1999).
- <sup>53</sup>C. D. Reintsema, J. S. Adams, R. Baker, S. R. Bandler, W. R. Doriese, E. Figueroa-Feliciano, G. C. Hilton, K. D. Irwin, R. L. Kelly, C. A. Kilbourne, J. W. Krinsky, F. S. Porter, and P. Wikus, *AIP Conf. Proc.* **1185**, 237–240 (2009).
- <sup>54</sup>C. D. Reintsema, J. Beyer, S. W. Nam, S. Deiker, G. C. Hilton, K. Irwin, J. Martinis, J. Ullom, L. R. Vale, and M. Macintosh, *Rev. Sci. Instrum.* **74**, 4500 (2003).
- <sup>55</sup>J. W. Fowler, B. K. Alpert, W. B. Doriese, Y.-I. Joe, G. C. O'Neil, J. N. Ullom, and D. S. Swetz, *J. Low Temp. Phys.* **184**, 374 (2016).
- <sup>56</sup>W. B. Doriese, K. M. Morgan, D. A. Bennett, E. V. Denison, C. P. Fitzgerald, J. W. Fowler, J. D. Gard, J. P. Hays-Wehle, G. C. Hilton, K. D. Irwin, Y. I. Joe, J. A. B. Mates, G. C. O'Neil, C. D. Reintsema, N. O. Robbins, D. R. Schmidt, D. S. Swetz, H. Tatsuno, L. R. Vale, and J. N. Ullom, *J. Low Temp. Phys.* **184**, 389 (2016).
- <sup>57</sup>C. Hagmann and P. L. Richards, *Cryogenics* **35**, 303 (1995).
- <sup>58</sup>V. K. Pecharsky and K. A. Gschneidner, Jr., *J. Magn. Magn. Mater.* **200**, 44 (1999).
- <sup>59</sup>C. Wang, G. Thummes, and C. Heiden, *Cryogenics* **37**, 159 (1997).
- <sup>60</sup>W. B. Doriese, J. S. Adams, G. C. Hilton, K. D. Irwin, C. A. Kilbourne, F. J. Schima, and J. N. Ullom, *AIP Conf. Proc.* **1185**, 450–453 (2009).
- <sup>61</sup>A. E. Szymkowiak, R. L. Kelley, S. H. Moseley, and C. K. Stahle, *J. Low Temp. Phys.* **93**, 281 (1993).
- <sup>62</sup>B. K. Alpert, R. D. Horansky, D. A. Bennett, W. B. Doriese, J. W. Fowler, A. S. Hoover, M. W. Rabin, and J. N. Ullom, *Rev. Sci. Instrum.* **84**, 056107 (2013).
- <sup>63</sup>D. J. Fixsen, S. H. Moseley, T. Gerrits, A. E. Lita, and S. W. Nam, *J. Low Temp. Phys.* **176**, 16 (2014).
- <sup>64</sup>B. Shank, J. J. Yen, B. Cabrera, J. M. Kreikebaum, R. Moffatt, P. Redl, B. A. Young, P. L. Brink, M. Cherry, and A. Tomada, *AIP Adv.* **4**, 117106 (2014).
- <sup>65</sup>S. E. Busch, J. S. Adams, S. R. Bandler, J. A. Chervenak, M. E. Eckart, F. M. Finkbeiner, D. J. Fixsen, R. L. Kelley, C. A. Kilbourne, S.-J. Lee, S. H. Moseley, J.-P. Porst, F. S. Porter, J. E. Sadleir, and S. J. Smith, *J. Low Temp. Phys.* **184**, 382 (2016).
- <sup>66</sup>P. Peille, M. T. Ceballos, B. Cobo, J. Wilms, S. Bandler, S. J. Smith, T. Dausser, T. Brand, R. den Hartog, J. de Plaa, D. Barret, J. W. den Herder, L. Piro, X. Barcons, and E. Pointecouteau, *Proc. SPIE* **9905**, 99055W (2016).
- <sup>67</sup>J. W. Fowler, B. K. Alpert, W. B. Doriese, J. Hays-Wehle, Y. I. Joe, K. M. Morgan, G. C. O'Neil, C. D. Reintsema, D. R. Schmidt, J. N. Ullom, and D. S. Swetz, *IEEE Trans. Appl. Supercond.* (published online).
- <sup>68</sup>S. G. Crowder, K. A. Barger, D. E. Brandl, M. E. Eckart, M. Galeazzi, R. L. Kelley, C. A. Kilbourne, D. McCammon, C. G. Pfendner, F. S. Porter, L. Rocks, A. E. Szymkowiak, and I. M. Teplin, *Astrophys. J.* **758**, 143 (2012).
- <sup>69</sup>P. A. B. Scoullar, C. C. McLean, and R. J. Evans, *AIP Conf. Proc.* **1412**, 270–277 (2011).
- <sup>70</sup>G. Hölzer, M. Fritsch, M. Deutsch, J. Härtwig, and E. Förster, *Phys. Rev. A* **56**, 4554 (1997).
- <sup>71</sup>C. T. Chantler, M. N. Kinnane, C.-H. Su, and J. A. Kimpton, *Phys. Rev. A* **73**, 012508 (2006).
- <sup>72</sup>J. W. Fowler, *J. Low Temp. Phys.* **176**, 414 (2014).
- <sup>73</sup>P. J. Green and B. W. Silverman, *Nonparametric Regression and Generalized Linear Models* (Chapman & Hall, 1994).
- <sup>74</sup>W. Fullagar, M. Harbst, S. Canton, J. Uhlig, M. Walczak, C.-G. Wahlström, and V. Sundström, *Rev. Sci. Instrum.* **78**, 115105 (2007).
- <sup>75</sup>B. Ravel, "Quantitative EXAFS analysis," in *X-Ray Absorption and X-Ray Emission Spectroscopy: Theory and Applications*, edited by J. A. van Bokhoven and C. Lamberti (John Wiley & Sons, Ltd., Chichester, UK, 2016), pp. 281–302.
- <sup>76</sup>J. Uhlig, "Life of a photon in x-ray spectroscopy," Ph.D. thesis, Lund University, 2011.
- <sup>77</sup>S. Mitsuya, H. Ishii, J. Kawai, and K. Tanaka, *Appl. Phys. Lett.* **89**, 134104 (2006).
- <sup>78</sup>G. Vankó, T. Neisius, G. Molnár, F. Renz, S. Kárpáti, A. Shukla, and F. M. F. de Groot, *J. Phys. Chem. B* **110**, 11647 (2006).
- <sup>79</sup>K. C. Kurien, *J. Chem. Soc. B* **2081** (1971).
- <sup>80</sup>C. J. Miles and P. L. Brezonik, *Environ. Sci. Technol.* **15**, 1089 (1981).
- <sup>81</sup>"XAFS Spectra Library."
- <sup>82</sup>R. Deslattes, E. Kessler, Jr., and P. Indelicato, *Rev. Mod. Phys.* **75**, 35 (2003).
- <sup>83</sup>B. Beckhoff, T. Jach, M. C. Lépy, and M. Mantler, Roadmap document on atomic fundamental parameters for X-ray methodologies, 2012.
- <sup>84</sup>J. Stöhr, *NEXAFS Spectroscopy*, Springer Series in Surface Sciences, edited by R. Gomer (Springer-Verlag, Berlin, 1996).
- <sup>85</sup>S. Friedrich, T. Funk, O. Drury, S. E. Labov, and S. P. Cramer, *Rev. Sci. Instrum.* **73**, 1629 (2002).
- <sup>86</sup>M. Ohkubo, S. Shiki, M. Ukibe, N. Matsubayashi, Y. Kitajima, and S. Nagamachi, *Sci. Rep.* **2**, 831 (2012).
- <sup>87</sup>U. Fano, *Phys. Rev.* **72**, 26 (1947).
- <sup>88</sup>S. Friedrich, J. Harris, W. K. Warburton, M. H. Carpenter, J. A. Hall, and R. Cantor, *J. Low Temp. Phys.* **176**, 553 (2014).
- <sup>89</sup>G. Fujii, M. Ukibe, S. Shiki, and M. Ohkubo, *J. Low Temp. Phys.* **184**, 194 (2016).
- <sup>90</sup>P. Verhoeve, D. D. E. Martin, and R. Venn, in *Proc. SPIE* **7742**, 774200 (2010).
- <sup>91</sup>S. Friedrich, F. Ponce, M. H. Carpenter, and R. Cantor, *Synchrotron Radiat. News* **27**, 28 (2014).
- <sup>92</sup>F. D. Vila, T. Jach, W. T. Elam, J. J. Rehr, and J. D. Denlinger, *J. Phys. Chem. A* **115**, 3243 (2011).
- <sup>93</sup>J. Fink, E. Schierle, E. Weschke, and J. Geck, *Rep. Prog. Phys.* **76**, 056502 (2013).
- <sup>94</sup>G. Ghiringhelli, M. Le Tacon, M. Minola, S. Blanco-Canosa, C. Mazzoli, N. B. Brookes, G. M. De Luca, A. Frano, D. G. Hawthorn, F. He, T. Loew, M. M. Sala, D. C. Peets, M. Salluzzo, E. Schierle, R. Sutarto, G. A. Sawatzky, E. Weschke, B. Keimer, and L. Braicovich, *Science* **337**, 821 (2012).
- <sup>95</sup>E. H. da Silva Neto, R. Comin, F. He, R. Sutarto, Y. Jiang, R. L. Greene, G. A. Sawatzky, and A. Damascelli, *Science* **347**, 282 (2015).
- <sup>96</sup>Ş. Smadici, P. Abbamonte, M. Taguchi, Y. Kohsaka, T. Sasagawa, M. Azuma, M. Takano, and H. Takagi, *Phys. Rev. B* **75**, 075104 (2007).
- <sup>97</sup>J. L. McChesney, R. Reininger, M. Ramanathan, C. Benson, G. Srajer, P. Abbamonte, and J. C. Campuzano, *Nucl. Instrum. Methods Phys. Res., Sect. A* **746**, 98 (2014).
- <sup>98</sup>G. Ghiringhelli, A. Piazzalunga, C. Dallera, G. Trezzi, L. Braicovich, T. Schmitt, V. N. Strocov, R. Betemps, L. Patthey, X. Wang, and M. Grioni, *Rev. Sci. Instrum.* **77**, 113108 (2006).
- <sup>99</sup>K. Jun, *Nucl. Instrum. Methods Phys. Res., Sect. B* **75**, 3 (1993).
- <sup>100</sup>C. J. Batty, E. Friedman, and A. Gal, *Phys. Rep.* **287**, 385 (1997).
- <sup>101</sup>T. Hashimoto, M. Bazzi, D. A. Bennett, C. Berucci, D. Bosnar, C. Curceanu, W. B. Doriese, J. W. Fowler, H. Fujioka, C. Guaraldo, F. P. Gustafsson, R. Hayakawa, R. S. Hayano, J. P. Hays-Wehle, G. C. Hilton, T. Hiraiwa, Y. Ichinohe, M. Iio, M. Iiesscu, S. Ishimoto, Y. Ishisaki, K. Itahashi, M. Iwasaki, Y. Ma, H. Noda, H. Nomi, G. C. O. Neil, H. Ohnishi, S. Okada, H. Outa, K. Piscicchia, C. Reintsema, Y. Sada, F. Sakuma, M. Sato, D. R. Schmidt, A. Scordo, M. Sekimoto, H. Shi, D. Sirghi, F. Sirghi, K. Suzuki, D. S. Swetz, K. Tanida, H. Tatsuno, M. Tokuda, J. Uhlig, J. N. Ullom, S. Yamada, T. Yamazaki, and J. Zmeskal, *IEEE Trans. Appl. Supercond.* (published online).
- <sup>102</sup>S. J. Smith, J. S. Adams, S. R. Bandler, G. Betancourt-Martinez, J. A. Chervenak, M. E. Eckart, F. M. Finkbeiner, R. L. Kelley, C. A. Kilbourne, S. J. Lee, F. S. Porter, J. E. Sadleir, and E. J. Wassell, *IEEE Trans. Appl. Supercond.* **25**, 2100505 (2015).
- <sup>103</sup>F. S. Porter, J. Gygas, R. L. Kelley, C. A. Kilbourne, J. M. King, P. Beiersdorfer, G. V. Brown, D. B. Thorn, and S. M. Kahn, *Rev. Sci. Instrum.* **79**, 10E307 (2008).
- <sup>104</sup>G. V. Brown, J. S. Adams, P. Beiersdorfer, J. Clementson, M. Frankel, S. M. Kahn, R. L. Kelly, C. A. Kilbourne, D. Koutroumpa, M. Leutenegger, F. S. Porter, D. B. Thorn, and E. Träbert, *AIP Conf. Proc.* **1185**, 446–449 (2009).
- <sup>105</sup>W. Holmes, J. M. Gildemeister, P. L. Richards, and V. Kotsubo, *Appl. Phys. Lett.* **72**, 2250 (1998).
- <sup>106</sup>J. P. Hays-Wehle, D. R. Schmidt, J. N. Ullom, and D. S. Swetz, *J. Low Temp. Phys.* **184**, 492 (2016).
- <sup>107</sup>G. Bortels and P. Collaers, *Int. J. Rad. Appl. Instrum. A* **38**, 831 (1987).
- <sup>108</sup>S. R. Bandler, R. P. Brekosky, A.-D. Brown, J. A. Chervenak, E. Figueroa-Feliciano, F. M. Finkbeiner, N. Iyomoto, R. L. Kelley, C. A. Kilbourne, F. S. Porter, J. Sadleir, and S. J. Smith, *J. Low Temp. Phys.* **151**, 400 (2008).
- <sup>109</sup>L. M. Gades, T. W. Cecil, R. Divan, D. R. Schmidt, J. N. Ullom, T. J. Madden, D. Yan, and A. Miceli, *IEEE Trans. Appl. Supercond.* (published online).

- <sup>110</sup>J. W. den Herder, D. Bagnali, S. Bandler, M. Barbera, X. Barcons, D. Barret, P. Bastia, M. Bisotti, K. Boyce, C. Cara, M. Ceballos, L. Corcione, B. Cobo, L. Colasanti, J. de Plaa, M. DiPirro, W. B. Doriese, Y. Ezoë, R. Fujimoto, F. Gatti, L. Gottardi, P. Guttridge, R. den Hartog, I. Hepburn, R. Kelley, K. Irwin, Y. Ishisaki, C. Kilbourne, P. A. J. de Korte, J. van der Kuur, S. Lotti, C. Macculi, K. Mitsuda, T. Mineo, L. Natalucci, T. Ohashi, M. Page, S. Paltani, E. Perinati, L. Piro, C. Pigot, F. S. Porter, G. Rauw, L. Ravera, E. Renotte, J.-L. Sauvageot, C. Schmid, S. Sciortino, P. Shirron, Y. Takei, G. Torrioli, M. Tsujimoto, L. Valenziano, D. Willingale, C. de Vries, H. van Weers, J. Wilms, and N. Y. Yamasaki, *Proceedings SPIE* **8443**, 84432B (2012).
- <sup>111</sup>K. D. Irwin, G. C. Hilton, D. A. Wollman, and J. M. Martinis, *J. Appl. Phys.* **83**, 3978 (1998).
- <sup>112</sup>D. A. Bennett, D. S. Swetz, R. D. Horansky, D. R. Schmidt, and J. N. Ullom, *J. Low Temp. Phys.* **167**, 102 (2012).
- <sup>113</sup>S. J. Lee, S. R. Bandler, S. E. Busch, J. S. Adams, J. A. Chervenak, M. E. Eckart, A. J. Ewin, F. M. Finkbeiner, R. L. Kelley, C. A. Kilbourne, J.-P. Porst, F. S. Porter, J. E. Sadleir, S. J. Smith, and E. J. Wassel, *J. Low Temp. Phys.* **176**, 597 (2014).
- <sup>114</sup>O. Noroozian, J. A. B. Mates, D. A. Bennett, J. A. Brevik, J. W. Fowler, J. Gao, G. C. Hilton, R. D. Horansky, K. D. Irwin, Z. Kang, D. R. Schmidt, L. R. Vale, and J. N. Ullom, *Appl. Phys. Lett.* **103**, 202602 (2013).
- <sup>115</sup>D. A. Bennett, J. A. B. Mates, J. D. Gard, A. S. Hoover, M. W. Rabin, C. D. Reintsema, D. R. Schmidt, L. R. Vale, and J. N. Ullom, *IEEE Trans. Appl. Supercond.* **25**, 2101405 (2015).
- <sup>116</sup>S. Doyle, "Detectors," *Synchrotron Radiat. News* **27**, 4 (2014).